communications earth & environment

Article

A Nature Portfolio journal

https://doi.org/10.1038/s43247-025-02923-9

Experimental constraints on the sources of lithium-rich granites and pegmatites

Bence Horányi[1] ✉, Austin M. Gion[1,2], Fabrice Gaillard[1], Éric Gloaguen[1,3], Alexis Plunder[3], Jérémie Melleton[3], Alban Moradell-Casellas[1,3], Josselyn Garde[1], Saskia Erdmann[1] & Ida Di Carlo[1]

Rare-metal granites and pegmatites are enriched in critical metals, such as lithium (>5000 ppm), relative to conventional granites in the crust (<100 ppm). The petrogenesis of lithium-bearing pegmatites has been historically associated with the high-degree fractional crystallisation of parental granites. However, the extent of lithium enrichment during this process remains debated due to uncertainties concerning the partitioning behaviour of lithium between minerals and felsic melts. Alternatively, lithium enrichment in granitic pegmatites may reflect the composition of their crustal source. To test the anatectic origin of rare-metal granites and pegmatites, partial melting experiments were performed on variably enriched metasedimentary rocks (100–800 ppm lithium). The experiments produced felsic melts with a lithium content of 180–2200 ppm and constrained mineral-melt partition coefficients for granitic systems. Trace element modelling demonstrates that high-grade granite-related deposits (>5000 ppm lithium) are sourced from the anatexis of enriched crustal rocks (>300 ppm lithium), followed by the moderate fractional crystallisation of the partial melts.

Granitic rocks have a diverse geochemical composition, which has been interpreted to reflect magmatic processes, such as fractional crystallisation, or the compositional diversity of their source material[1]. A notable example of this variability is the range of lithium contents observed in peraluminous granites. An end-member of this compositional range constitutes rare-metal granites and pegmatites (RMGPs; Fig. 1a), which are regarded as important deposits of lithium (up to 11,800 ppm[2]) and other rare metals (Rb, Cs, Ta, W, and Nb). Lithium is of particularly high economic interest due to its rising demand for modern-day technologies, such as batteries. Approximately 60% of the global lithium supply is sourced from granitic pegmatites[2]. These deposits are enriched by over two orders of magnitude relative to the median composition of peraluminous granites in the crust (25 ppm; Fig. 1b). The elevated lithium content of RMGPs has been historically associated with the high-degree fractional crystallisation of residual felsic melts extracted from a parental granite[3–5]. Alternative hypotheses propose that RMGPs form by the direct anatexis of metasedimentary rocks or orthogneisses[6–9]. Thus, the enrichment of lithium in RMGPs may reflect the composition of their crustal source, in addition to magmatic evolution (Fig. 1a).

Recent studies have proposed that RMGPs form in a two-stage process, involving both anatexis and fractionation[10–13]. In the first stage of RMGP genesis, the low-degree (<10%) partial melting of metasedimentary rocks produces a lithium-rich, felsic melt[10,11,13]. In the second stage, these partial melts undergo high-degree fractional crystallisation (80–99%) to produce RMGPs[10,11]. Alternatively, the extracted melts may first crystallise to form a granitic pluton and re-melt during a second anatectic event[12,13]. Low-degree (7%) partial melts may then get extracted and crystallise to form RMGPs.

Although these models constitute considerable progress in the understanding of RMGP genesis, several limitations impede their application. Firstly, the mechanism of low-degree melt extraction remains debated in the literature. The efficiency of residual melt extraction in highly fractionated granitic systems (>70–75% crystallinity) is impeded by the development of a low-permeability crystalline framework[14,15]. Secondly, the validity of petrogenetic models relies on the accuracy of mineral-melt partition coefficients. Experimental partition coefficients of lithium between minerals and granitic melts are scarce and vary considerably as a function of crystallisation conditions, as well as the composition of minerals and melts (Supplementary Data 1)[16–23]. The use of these partition coefficients may lead to strikingly different interpretations of lithium enrichment during RMGP genesis. Lastly, the geochemically diverse crustal source of peraluminous granites remains poorly explored. Previous studies have considered the anatexis of metapelites and gneisses that are moderately enriched in rare metals (~50–270 ppm lithium) relative to the median composition of metasedimentary rocks in the crust (20 ppm lithium; Fig. 1b)[10,11,13,24,25]. To better understand the enrichment of lithium during crustal anatexis, it is important to also consider the partial melting of enriched metasedimentary rocks that are observed in nature (Fig. 1b).

[1]Institute des Sciences de la Terre d'Orléans, UMR 7327, Université d'Orléans, CNRS, BRGM, OSUC, Orléans, France. [2]Department of Earth Sciences, University of Oxford, Oxford, UK. [3]Bureau de Recherches Géologiques et Minières, Orléans, France. ✉e-mail: bence.horanyi@cnrs-orleans.fr

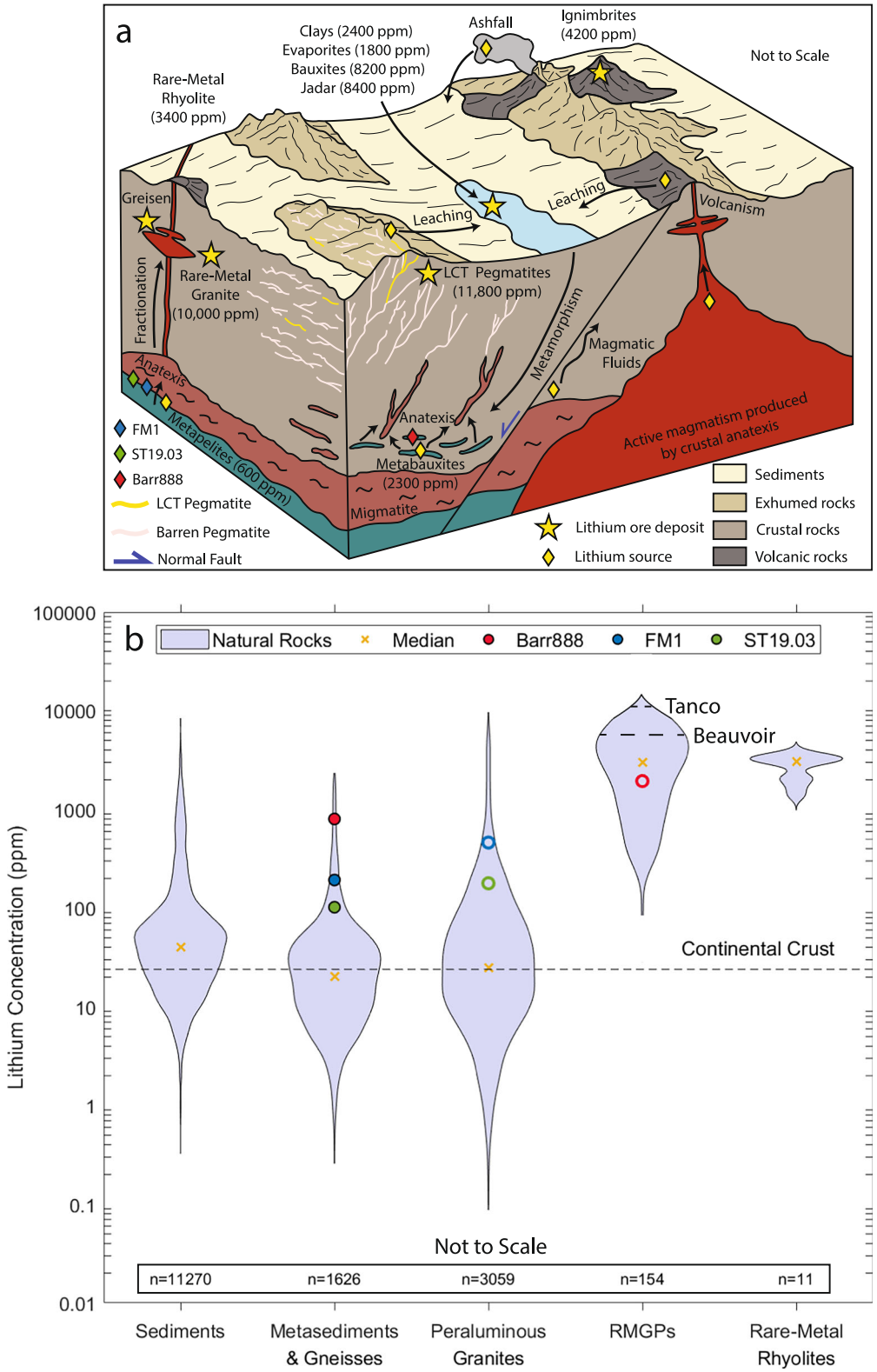

Fig. 1 | The lithium cycle in the continental crust. a The distribution and possible cycling of lithium between magmatic, sedimentary, and metamorphic reservoirs (modified from Gloaguen et al.[29] and Lefebvre and Tavignot[70]). Numbers in brackets indicate the highest recorded lithium content in each deposit (Supplementary Data 2)[2]. **b** Violin plots of the lithium distribution in various crustal reservoirs (see Supplementary Data 2). Filled and open circles represent the composition of the starting materials and the mean composition of the glasses from the low-degree, fluid-absent partial melting experiments, respectively. Error bars, defined as the standard deviation of the mean ($1\sigma_m$), are smaller than the size of the symbols. '*n*' denotes the number of analyses.

Lithium can accumulate in clay, evaporite, bauxite, and altered volcano-sedimentary deposits, which contain up to ~2500, ~2000, ~8200, and ~8400 ppm lithium, respectively[2,26–28] (Fig. 1b). These sedimentary rocks may undergo metamorphism, during which ~20–50% of the bulk lithium content can be removed by devolatilisation[29]. The medium to high-grade metamorphism of enriched protoliths produces metabauxites, metapelites, paragneisses, granulites, metavolcanic rocks, amphibolites, metagraywackes, and orthogneisses, containing up to 2290, 600, 560, 280, 260, 240, 210, and 160 ppm lithium, respectively (see Supplementary Note and Supplementary Data 2). In metasedimentary rocks, lithium is primarily hosted in staurolite, followed by cordierite, biotite, muscovite, garnet, and tourmaline[30]. Staurolite is typically considered to be absent during the onset of partial melting due to its subsolidus breakdown at ~650 °C[31]. However, experimental, analytical, and numerical studies have demonstrated that staurolite can contribute to melting reactions during crustal anatexis, particularly in lithium-rich metapelites (see Supplementary Discussion). The partial melting of enriched, staurolite-bearing metasedimentary rocks may produce lithium-rich melts that crystallise to form RMGPs or rare-metal rhyolites[32].

To test the anatectic origin of RMGPs, partial melting and crystallisation experiments were performed on two micaschists (ST19.03 and FM1) and a metabauxite (Barr888), with bulk lithium contents of 102, 193, and 800 ppm, respectively (Fig. 1b). The partial melting experiments were conducted in either a piston-cylinder apparatus or an internally heated pressure vessel at 750–800 °C and 400–1000 MPa, for up to 430 h (Table 1). Crystallisation experiments were performed under the same conditions to identify whether equilibrium has been attained. All experiments were performed either at fluid-absent (no added H_2O) or fluid-present conditions (10 wt% added H_2O) to investigate the effect of the degree of melting on lithium enrichment. Minerals and glasses in run products were imaged by scanning electron microscopy, whereas their major and trace element compositions were determined by electron probe microanalysis and laser ablation inductively coupled plasma mass spectrometry, respectively (Supplementary Fig. 1; Tables S1 and S2 in Supplementary Data 1). The experimental results demonstrate that the rare metal content of partial melts varies as a function of the starting material composition, the degree of melting, and the partitioning of rare metals into residual or newly crystallising minerals. The enrichment of lithium during crustal anatexis was further investigated by trace element modelling using newly constrained mineral-melt partition coefficients and the modal mineralogy of the experimental run products, determined by mass balance calculations (Tables S3 and S4 in Supplementary Data 1). The modelled results are consistent with RMGPs being sourced from enriched crustal rocks. The partial melts produced by anatexis may become further enriched in lithium and other rare metals during fractional crystallisation, the re-melting of granitic plutons, or late-stage metasomatic processes.

Results

Starting materials

The FM1 and ST19.03 micaschists formed by the high-grade (amphibolite facies) metamorphism of a pelitic protolith in the Variscan orogenic belt[33], whereas the Barr888 metabauxite formed at upper greenschist facies conditions in a subduction zone setting[34]. The metasedimentary samples are composed of an assemblage of staurolite + muscovite + quartz + rutile ± biotite ± margarite ± garnet ± plagioclase ± ilmenite ± kyanite ± pyrophillite (Fig. 2; Tables S5 and S6 in Supplementary Data 1). The ST19.03 micaschist is weakly enriched in Li, Rb, Cs, Ta, Nb, and W, whereas FM1 is moderately enriched in all rare metals relative to the median composition of metasedimentary rocks in nature (Fig. 1b and Table 2). In contrast, the Barr888 metabauxite has a relatively low rubidium and caesium content; however, it is highly enriched in Li, Ta, Nb, and W relative to conventional metasedimentary rocks (Fig. 1b and Table 2). Lithium is primarily hosted in staurolite, followed by margarite, biotite, garnet, and muscovite (Fig. 2 and Table S7 in Supplementary Data 1). In the micaschists, Rb, Cs, Nb, and Ta are principally hosted in biotite, whereas tungsten is predominantly found in muscovite (Table S7 in Supplementary Data 1). Ilmenite and rutile are enriched in Nb, Ta, and W, particularly in Barr888, wherein biotite is absent. In the metabauxite, rare metals are almost exclusively hosted in staurolite, micas, and oxides, which can remain stable during high-grade metamorphism[35]. Thus, the bulk lithium content of Barr888 is interpreted to be representative of lithium enrichment in high-grade metabauxites.

Experimental run products

The experiments produced a felsic melt ± staurolite ± quartz ± plagioclase ± sillimanite ± rutile ± biotite ± cordierite ± tourmaline ± garnet ± magnetite ± Fe–Ti oxides ± hercynite ± gahnite ± alkali feldspar ± corundum (Fig. 3 and Table 1). The degree of melting varies from 15–35% in the fluid-absent melting experiments to 60–80% in all crystallisation and fluid-present melting experiments (Tables 2, S3 and S8 in Supplementary Data 1). Partial melting of the metasedimentary rocks is primarily driven by the breakdown of muscovite (± margarite) in a schematic reaction that forms a melt, alkali feldspar (± plagioclase), and sillimanite[36] (Fig. 3a and b):

$$\mathrm{Muscovite_{(res)} + Plagioclase_{(res)} + Quartz_{(res)} \rightarrow Melt + Alkali\ Feldspar_{(new)} + Sillimanite_{(new)}} \quad (1)$$

Newly crystallising biotite is absent in all partial melting run products, which is consistent with previous experimental studies conducted on metapelites[36]. Residual biotite (± garnet) partially breaks down in the fluid-absent melting experiments (Fig. 3c and d), which produces a melt + cordierite + magnetite (± tourmaline):

$$\mathrm{Biotite_{(res)} + Sillimanite_{(new)} + Plagioclase_{(res)} + Quartz_{(res)} \rightarrow Melt + Cordierite_{(new)} + Magnetite_{(new)}} \quad (2)$$

Staurolite is a residual phase in the fluid-absent and fluid-present partial melting experiments (Table 1). In the Barr888 experimental run products, staurolite partially breaks down to form a melt, sillimanite, and hercynite or gahnite (Fig. 3e):

$$\mathrm{Staurolite_{(res)} + Muscovite_{(res)} \rightarrow Melt + Sillimanite_{(new)} \pm Hercynite_{(new)} \pm Gahnite_{(new)}} \quad (3)$$

In the FM1 and ST19.03 experiments, ilmenite breaks down to form intergrowths of magnetite and rutile pseudomorphs (Fig. 3f). This reaction is interpreted to be a function of the increasingly oxidising conditions of the experiments following the dissociation of water to H_2, and the outward diffusion of hydrogen through the capsules[37]:

$$\mathrm{Ilmenite_{(res)} + Water \rightarrow Rutile_{(new)} + Magnetite_{(new)} + Hydrogen} \quad (4)$$

The Barr888 experiments were buffered at CCO by the presence of carbon and sulfur in the accessory minerals ankerite and pyrite, respectively[37]. Therefore, magnetite is absent in the reducing experiments performed on the Barr888 metabauxite.

In the fluid-present melting experiments, muscovite, biotite, and garnet completely break down, as illustrated by the schematic Eqs. (1) and (2) (Fig. 3g). Plagioclase is also consumed in these reactions; therefore, feldspars are absent in the run products of the fluid-present melting experiments. Corundum crystallises following the complete or partial breakdown of pelitic minerals (micas, garnet, and staurolite), which indicates that the melt is saturated in Al_2O_3.

Staurolite is absent in all crystallisation experiments (Fig. 3h), which demonstrates that it is unstable during low-temperature (750–800 °C) crustal anatexis. The breakdown of staurolite results in the crystallisation of hercynite ± gahnite ± sillimanite ± corundum (see schematic Eq. (3) and Supplementary Fig. 2). Garnet and feldspars are absent, whereas biotite is

https://doi.org/10.1038/s43247-025-02923-9

Table 1 | Experimental conditions and run products

Run	Starting material	Apparatus[a]	Temperature (°C)	Pressure (MPa)	Duration (h)	H_2O added (wt%)	Newly formed phases	Residual phases
High-temperature melting								
PC1	Barr888	PC	1000	700	96	0	Gl + Pl + Gnt + Sill + Crn + Rt	St
PC2	Barr888	PC	1200	1000	48	0	Gl + Sill + Crn	n.a.[b]
A1	Barr888	IHPV	1200	400	48	10	Gl +Sill + Crn	n.a.
BH_MSed1	FM1	IHPV	1200	200	72	0	Gl +Crn + Hc	n.a.
BH_MSed4	ST19.03	IHPV	1200	200	72	0	Gl +Crn + Hc	n.a.
Fluid-absent melting								
GAR01	FM1	PC	750	700	330	0	Gl + Crd + Tur + Afs + Sill + Rt + Mag	St + Bt + Grt + Qz + Pl
GAR09	ST19.03	PC	750	700	69	0	Gl + Crd + Afs + Sill + Rt + Mag	St + Bt + Grt + Qz + Pl
PC5	Barr888	PC	750	700	144	0	Gl + Pl + Afs + Sill + Crn + Aln + Rt + Fe–Ti oxide[c]	St + Qz
PC3	Barr888	PC	800	700	168	0	Gl + Pl + Afs + Sill + Crn + Aln + Rt + Fe–Ti oxide	St + Qz
PC7 F	Barr888	PC	800	700	168	0	Gl + Pl + Afs + Sill + Crn + Aln + Rt + Fe–Ti oxide	St + Qz
PC8 F	Barr888	PC	800	1000	168	0	Gl + Pl + Afs + Sill + Crn + Aln + Rt + Fe–Ti oxide	St + Qz
A2 F	Barr888	IHPV	800	400	120	0	Gl + Pl + Hc + Sill + Crn + Aln + Rt + Fe–Ti oxide	St + Qz
A3	Barr888	IHPV	800	400	48	0	Gl + Pl + Hc + Sill + Crn + Aln + Rt + Fe–Ti oxide	St + Qz
Fluid-present melting								
GAR02	FM1	PC	750	700	330	10	Gl + Crd + Tur + Sill + Crn + Rt + Mag	St + Qz
GAR03	FM1	PC	750	700	330	10	Gl + Crd + Tur + Sill + Crn + Rt + Mag	St + Qz
Fluid-absent crystallisation								
GAR05	FM1	PC	750	700	72	0	Gl + Bt + Hc + Sill + Crn	St + Qz
GAR08	FM1	PC	750	700	72	0	Gl + Bt + Hc + Sill + Crn	St + Qz
GAR13	FM1	PC	750	700	430	0	Gl + Bt + Hc + Sill	n.a.
PC7 C	A1 Glass	PC	800	700	168	0	Gl + Pl + Afs + Hc + Sill + Crn + Fe–Ti oxide	Qz
PC8 C	A1 glass	PC	800	1000	168	0	Gl + Pl + Bt + Hc + Sill + Crn + Fe–Ti oxide	Qz
A2 C	A1 Glass	IHPV	800	400	120	0	Gl + Pl + Hc + Sill + Crn + Fe–Ti oxide	Qz
A4	A1 Glass	IHPV	800	400	168	0	Gl + Pl + Hc + Sill + Crn + Fe–Ti oxide	Qz
Fluid-present crystallisation								
GAR06	FM1	PC	750	700	72	10	Gl + Bt + Hc + Sill + Crn	St + Qz
GAR07	FM1	PC	750	700	72	10	Gl + Bt + Hc + Sill + Crn	St + Qz
GAR15	FM1	PC	750	700	430	10	Gl + Bt + Hc	n.a.

Afs alkali feldspar, *Bt* biotite, *Crd* cordierite, *Crn* corundum, *Gl* glass, *Gnt* gahnite, *Grt* garnet, *Hc* hercynite, *Mag* magnetite, *Pl* plagioclase, *Qz* quartz, *Rt* rutile, *Sill* sillimanite, *St* staurolite, *Tur* tourmaline. Headings in italic highlight the experimental procedure.

[a]PC = piston-cylinder (oxygen fugacity = ~CCO), IHPV = internally heated pressure vessel (oxygen fugacity = ~QFM).

[b]n.a. = not applicable.

[c]Fe–Ti oxides are too small to be precisely identified.

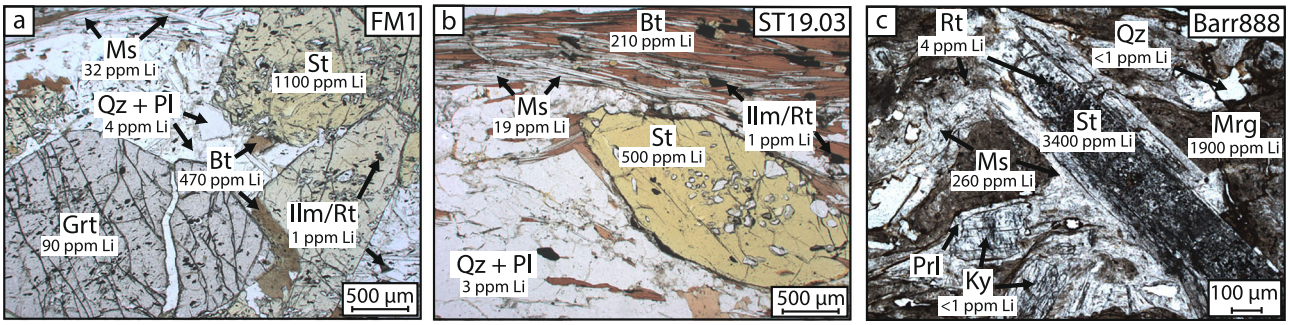

Fig. 2 | Representative thin-section images of the starting materials and the distribution of lithium between minerals. a FM1 micaschist. **b** ST19.03 micaschist. **c** Barr888 metabauxite. Bt = biotite, Grt = garnet, Ilm = ilmenite, Ky = kyanite, Mrg = margarite, Ms = muscovite, Pl = plagioclase, Prl = pyrophyllite, Qz = quartz, Rt = rutile, St = staurolite.

stable in all FM1 crystallisation run products (Fig. 3i). Plagioclase ± alkali feldspar ± biotite + Fe–Ti oxides are also present in the crystallisation experiments of the Barr888 metabauxite (Table 1).

The melting reactions observed in the experiments (see schematic Eqs. (1)–(4)) have a pronounced effect on the modal mineralogy of the run products. The partial melting of the metasedimentary rocks is associated with the decrease in the modal proportion of residual staurolite, biotite, muscovite, garnet, plagioclase, quartz, and ilmenite, as well as the increase in the proportion of newly crystallising cordierite, tourmaline, alkali feldspar, hercynite, rutile, magnetite, and sillimanite in the run products compared to the starting materials (Supplementary Fig. 3 and Table S3 in Supplementary Data 1). The complete breakdown of biotite and garnet in the fluid-present melting experiments is consistent with the increased proportion of cordierite, tourmaline, and melt in the run products (Supplementary Fig. 3).

Major element composition of partial melts

The major element compositions of the glasses in the fluid-absent melting, fluid-present melting, and crystallisation experiments are comparable to the geochemical signature of RMGPs and melts produced in previous experimental studies[25,35,36] (Table 2 and Supplementary Figs. 4 and 5). All glasses are interpreted to be fluid under-saturated, containing <10 wt% water, which is consistent with anatectic granites observed in nature[38]. The partial melts are marked by their elevated SiO_2, Al_2O_3, Na_2O, and K_2O contents, as well as their low TiO_2, FeO, MgO, and MnO contents, which is characteristic of evolved granitic rocks (Table 2). The melts are also highly peraluminous, with an aluminium saturation index (ASI, defined as the molar ratio of Al_2O_3 to Na_2O, K_2O, and CaO) of 1.2–1.4, which is similar to the ASI of RMGPs (Table 2). Fluxing components (F and P_2O_5) and the Na_2O/K_2O ratio of the experimental glasses are depleted relative to RMGPs; however, they are consistent with previous experimental studies[35,36]. The Na_2O/K_2O ratio of RMGPs is interpreted to be higher due to the crystallisation of alkali feldspar and biotite during fractionation[39] or the late-stage metasomatic alteration of alkali feldspar to albite[40]. Fluxing components may also become further enriched during fractional crystallisation or late-stage metasomatic processes[10].

The enrichment of rare metals during crustal anatexis

The partial melting of the metasedimentary rocks produced a melt that is enriched in Li, Rb, and Cs, whereas the glass is depleted in Nb, Ta, and W relative to the starting materials (Fig. 4). The experimental results demonstrate that rare metal endowment in the partial melts is most pronounced during the anatexis of enriched crustal rocks. The enrichment of rare metals can be further enhanced or limited by the partitioning of trace elements between minerals and melts, which can be estimated using mineral-melt partition coefficients ($D_i^{\text{Mineral/Melt}}$):

$$D_i^{\text{Mineral/Melt}} = \frac{C_i^{\text{Mineral}}}{C_i^{\text{Melt}}}, \quad (5)$$

where C_i^{Mineral} is the concentration of a trace element in the mineral and C_i^{Melt} is the concentration of a trace element in the melt. Partition coefficients of Li, Rb, Ta, Nb, and W are comparable between fluid-absent melting, fluid-present melting, and crystallisation experiments, which demonstrates an approach to equilibrium (see Supplementary Discussion). Due to the incompatible nature of the rare metals, the glasses produced by the low-degree, fluid-absent melting experiments are inherently more enriched relative to the high-degree, fluid-present melting and crystallisation experiments (Table S8 in Supplementary Data 1). Furthermore, residual minerals are generally depleted in Li, Rb, Cs, Ta, Nb, and W relative to the composition of the minerals in the starting materials. These elements either partition into the melt or into newly formed minerals, such as cordierite, tourmaline, alkali feldspar, rutile, and magnetite.

The glasses in the fluid-absent melting experiments are enriched in rubidium (up to 432 ppm) and caesium (up to 130 ppm) relative to the starting materials by a factor of ~2–3 following the breakdown of white micas and the partial breakdown of biotite (Fig. 4 and Table 2). Enrichment in the melt is limited by the partitioning of rubidium and caesium into residual biotite ($D_{\text{Rb,Cs}}^{\text{Bt/Melt}} = 1.8–2.0$), as well as newly crystallising alkali feldspar ($D_{\text{Rb}}^{\text{Afs/Melt}} = 0.79$) and cordierite ($D_{\text{Cs}}^{\text{Crd/Melt}} = 0.34$) produced by incongruent melting (Table 3). The rubidium and caesium content of the partial melts produced by the FM1 fluid-absent melting experiments is consistent with weakly enriched RMGPs; however, it is depleted relative to high-grade deposits (Fig. 4).

Tantalum (<1 ppm), Nb (<14 ppm), and W (<7 ppm) are depleted in the partial melts relative to the starting materials due to the crystallisation of rutile and magnetite in the FM1 and ST19.03 experiments (Fig. 4 and Table 3). Tantalum and niobium are highly compatible in rutile ($D_{\text{Ta}}^{\text{Rt/Melt}} = 130$, $D_{\text{Nb}}^{\text{Rt/Melt}} = 75$) and magnetite ($D_{\text{Ta}}^{\text{Mag/Melt}} = 17$, $D_{\text{Nb}}^{\text{Mag/Melt}} = 12$), whereas tungsten is also compatible in magnetite ($D_{\text{W}}^{\text{Mag/Melt}} = 6.6$). In contrast to the Barr888, FM1, and ST19.03 experiments, the partial melting of an orthogneiss by Michaud et al.[25] produced a melt that is enriched in Ta, Nb, and W by a factor of ~1.5–3.5 relative to its starting composition. The enrichment of these elements is interpreted to be a function of the oxygen fugacity of the experiments. At reducing conditions in natural systems[41] and in the experiments of Michaud et al.[25], ilmenite is stable, wherein Ta, Nb, and W are depleted relative to rutile and magnetite (see Supplementary Data 3). Therefore, the anatexis of enriched crustal rocks at reducing conditions can produce melts with a niobium and tungsten signature that is comparable to RMGPs (Fig. 4). In contrast, tantalum is depleted relative to RMGPs in all experimental run products.

The enrichment of lithium during crustal anatexis

The complete breakdown of white micas and the partial breakdown of staurolite ± biotite, produced a melt with 180–2200 ppm lithium (Fig. 1b). The enrichment of lithium is most pronounced in the fluid-absent melting experiments, wherein the glasses are enriched by a factor of ~2–3 relative to

Table 2 | Representative major and trace element compositions of the starting materials, experimental glasses, and RMGs

	Starting materials			Fluid-absent melting experiments			RMGPs
Sample	**FM1**	**ST19.03**	**Barr888**	**GAR 01**	**GAR 09**	**A2 F**	**RMGs**
wt%	***n* = 10**	***n* = 10**	***n* = 12**	***n* = 19**	***n* = 11**	***n* = 3**	***n* = 127**
SiO_2	63.7 (4)	61.2 (3)	45.3 (9)	71 (1)	73.3 (7)	68.4 (3)	70 (2)
TiO_2	0.82 (2)	0.94 (4)	1.99 (9)	0.14 (6)	0.13 (3)	0.29 (1)	b.d. to 0.02
Al_2O_3	17.1 (2)	18.6 (3)	35 (1)	12.7 (5)	12.7 (3)	14.7 (2)	16.4 (9)
$FeO_{(t)}$	7.0 (2)	6.7 (1)	2.3 (2)	1.3 (4)	0.44 (6)	1.1 (1)	0.4 (2)
MgO	2.11 (6)	2.40 (6)	0.25 (3)	0.3 (1)	0.11 (3)	0.10 (1)	0.2 (2)
MnO	0.17 (3)	0.08 (3)	n.a.[a]	0.11 (3)	0.02 (2)	b.d.[b]	b.d. to 0.35
CaO	0.23 (2)	0.25 (2)	3.3 (1)	0.38 (6)	0.17 (1)	0.99 (2)	0.6 (6)
Na_2O	1.01 (8)	2.05 (7)	1.29 (7)	1.9 (4)	2.8 (2)	1.2 (4)	4.3 (8)
K_2O	3.89 (8)	3.67 (7)	2.3 (1)	5.6 (5)	5.2 (1)	6.2 (3)	3.3 (6)
ZnO	n.a.	n.a.	0.4 (1)	n.a.	0.04 (2)	0.0902 (6)	n.a.
P_2O_5	0.11 (4)	0.14 (3)	0.03 (2)	0.16 (8)	0.15 (5)	0.04 (2)	2 (1)
F	b.d.	b.d.	b.d.	0.06 (5)	0.2 (1)	0.46 (6)	2 (1)
Cl	0.02 (1)	0.010 (6)	n.a.	0.22 (3)	0.006 (4)	n.a.	n.a.
–(F,Cl) = O	0.005 (3)	0.002 (1)	b.d.	b.d. to 0.02	0.08 (5)	0.20 (3)	0.7 (5)
Total	96.1 (5)	96.0 (4)	92 (1)	94 (2)	95.0 (6)	93.2 (6)	98 (1)
ppm	***n* = 10**	***n* = 10**	***n* = 16**	***n* = 13**	***n* = 7**	***n* = 8**	***n* = 127**
Li	193 (3)	102 (1)	800 (40)	470 (30)	180 (10)	1900 (80)	3000 (2000)
Rb	224 (2)	138 (2)	80 (4)	432 (6)	240 (20)	235 (8)	3000 (1000)
Nb	14.4 (2)	10.9 (3)	37 (2)	13 (2)	8 (2)	2.1 (9)	90 (30)
Cs	49.5 (5)	6.9 (1)	8.1 (0.3)	130 (20)	12.3 (5)	25 (2)	300 (200)
Ta	0.91 (6)	0.70 (5)	2.5 (1)	0.8 (3)	0.5 (1)	0.2 (1)	200 (100)
W	1.5 (2)	0.9 (1)	6.2 (4)	2 (1)	1.2 (5)	3 (1)	40 (30)
Bulk D_{Li}[c]	n.a.	n.a.	n.a.	0.15	0.22	0.22	n.a.
Bulk D_{Rb}	n.a.	n.a.	n.a.	0.34	0.37	0.004	n.a.
Bulk D_{Nb}	n.a.	n.a.	n.a.	1.84	1.95	2.29	n.a.
Bulk D_{Cs}	n.a.	n.a.	n.a.	0.22	0.29	0.004	n.a.
Bulk D_{Ta}	n.a.	n.a.	n.a.	2.05	2.30	4.01	n.a.
Bulk D_W	n.a.	n.a.	n.a.	0.44	0.39	0.01	n.a.
ASI[d]	**n.a.**	**n.a.**	**n.a.**	**1.3 (1)**	**1.21 (4)**	**1.4 (1)**	**1.5 (2)**
Melt Fraction	**n.a.**	**n.a.**	**n.a.**	**18%**	**25%**	**34%**	**n.a.**

Detailed major and trace element compositions of glasses are reported in Table S8 in Supplementary Data 1. Composition of 'PHP' RMGs is taken from Linnen and Cuney[5]. Uncertainty is reported to the last digit(s) in the brackets as the standard deviation of the mean ($1\sigma_m$). '*n*' denotes the number of analyses.

[a]n.a. = not analysed.

[b]b.d. = below detection.

[c]Bulk partition coefficients are calculated using Eq. (6).

[d]ASI is calculated as the molar ratio of Al2O3/($Na_2O + K_2O + (CaO - \frac{1}{3}P_2O_5)$).

their metasedimentary source. Conversely, the glasses produced by all crystallisation and fluid-present melting experiments are enriched in lithium by a factor of ~1.1–1.5 (Table S8 in Supplementary Data 1) due to the dilution of incompatible elements during high-degree melting[42]. The degree of lithium enrichment is consistent between the reducing (Barr888) and oxidising (FM1 and ST19.03) experiments, which demonstrates that oxygen fugacity has a negligible effect on lithium endowment during crustal anatexis. The lithium content of the glasses produced by the partial melting of Barr888 is comparable to moderately enriched RMGPs; however, they are depleted relative to high-grade deposits, such as the most evolved 'B1' unit of the Beauvoir granite (5800 ppm[43]) or the Tanco pegmatite (11,800 ppm[2]). The enrichment of lithium in the partial melts may be furthered following the complete breakdown of rare-metal-bearing minerals, such as biotite and staurolite, assuming that the latter is stable or metastable during the onset of melting. Lithium is enriched in these residual phases (along with garnet, and plagioclase) relative to newly crystallising minerals (e.g., cordierite, tourmaline, and alkali feldspar), which demonstrates that lithium primarily partitions into the melt during anatexis (Tables 3, S9–S11 in Supplementary Data 1). For example, the incongruent melting of staurolite produces minerals that are depleted in rare metals (sillimanite ± hercynite ± gahnite; Table 3); therefore, lithium is predominantly incorporated into the melt. In comparison, the dehydration melting of muscovite and biotite (+ plagioclase ± garnet ± quartz ± sillimanite) produces cordierite and alkali feldspar (± magnetite ± sillimanite), which can sequester rare metals in the run products (Table 3). Lithium also partitions into residual plagioclase (Table 3), which may further limit enrichment during anatexis[44].

The partitioning of lithium between minerals and melts

Lithium is moderately incompatible in staurolite, biotite, plagioclase, cordierite, garnet, and alkali feldspar ($D_{Li}^{Mineral/Melt} = 0.2–0.5$), whereas it is highly incompatible in tourmaline, hercynite, magnetite, rutile, and quartz ($D_{Li}^{Mineral/Melt} = 0.01–0.1$; Fig. 5). The $D_{Li}^{Mineral/Melt}$ obtained in this study are consistent with previous experimental partition coefficients[16–23] and are

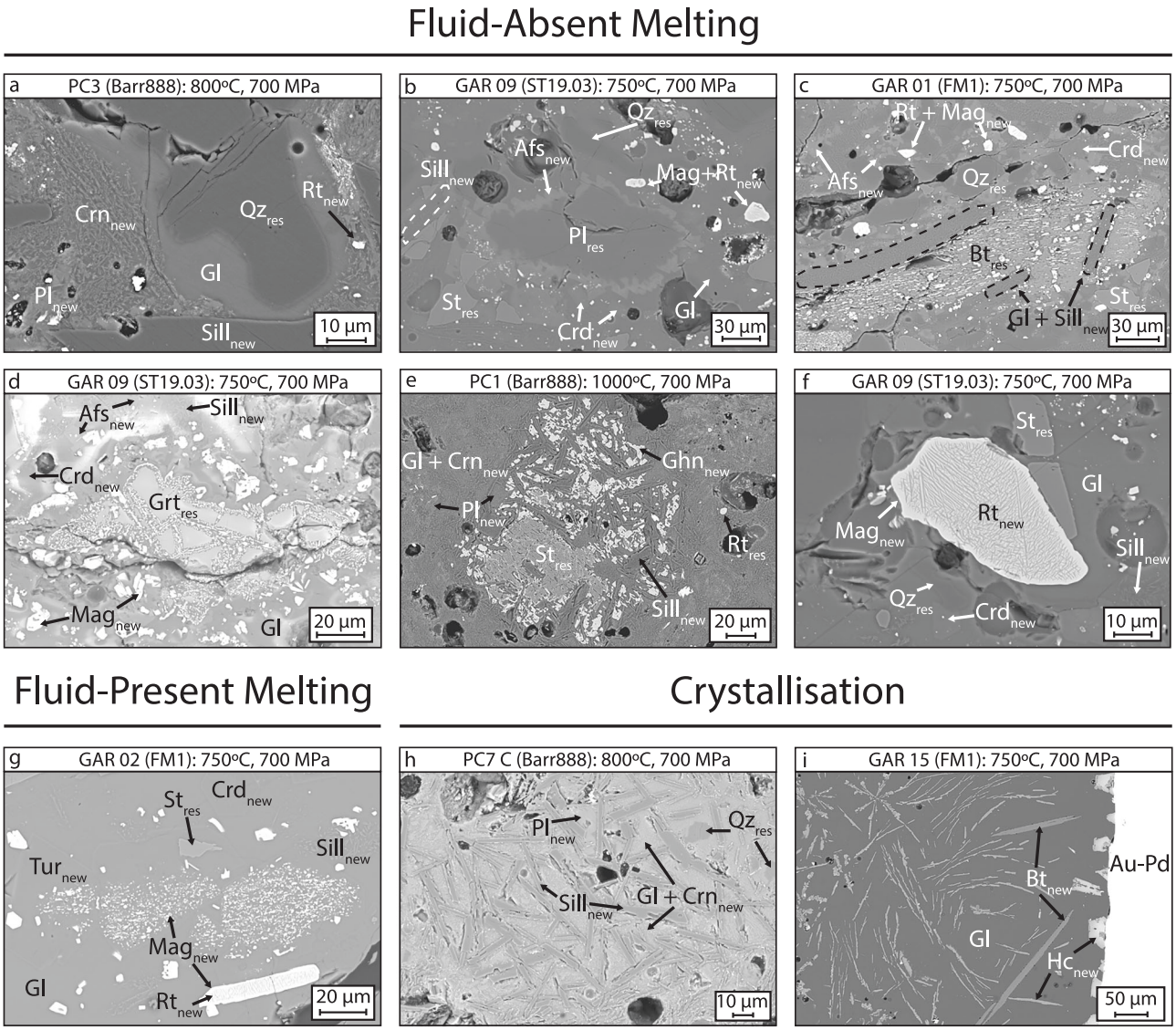

Fig. 3 | Representative scanning electron microscopy images of mineral textures in the experimental run products. a Melt pockets next to residual quartz phenocrysts. **b** The replacement of residual plagioclase rims with newly crystallising alkali feldspar. **c** The breakdown of muscovite to sillimanite and melt, and the exsolution of magnetite from residual biotite. **d** The incomplete breakdown of garnet to cordierite, magnetite, and melt. **e** The partial breakdown of staurolite to gahnite, sillimanite, and melt. **f** Rutile and magnetite intergrowths in pseudomorphs of ilmenite. **g** The complete breakdown of biotite to garnet, tourmaline, magnetite, and melt in the fluid-present melting experiments. **h** Representative mineralogy of Barr888 crystallisation experiments. **i** Representative mineralogy of the FM1 crystallisation experiments. Afs = alkali feldspar, Bt = biotite, Crd = cordierite, Crn = corundum, Ghn = gahnite, Gl = glass, Grt = garnet, Hc = hercynite, Mag = magnetite, Pl = plagioclase, Qz = quartz, Rt = rutile, Sill = sillimanite, St = staurolite. 'res' denotes residual phases, whereas 'new' signifies newly crystallised minerals.

largely consistent with $D_{Li}^{Mineral/Melt}$ derived from migmatites and rhyolites[10,44–48] (Fig. 5).

Partition coefficients derived from granites and pegmatites[49,50] were not considered in this study because of several limitations that hinder their application to magmatic processes. Firstly, lithium-rich pegmatites form by disequilibrium crystallisation at a low temperature (<600 °C[22]) compared to anatectic regimes in nature (>750 °C), which likely influences the partitioning behaviour of trace elements[51]. Secondly, lithium behaves as a major element in micas in RMGPs; therefore, conventional partition coefficients derived from zinnwaldite or lepidolite are not representative due to the non-Henry's law behaviour of lithium[52]. Lastly, the redistribution of trace elements during post-magmatic metasomatic processes may overprint the geochemical signature of granites and pegmatites[40], which likely results in considerable variability in apparent partition coefficients. The high mobility of lithium during late-stage processes is also reflected by the range of partition coefficients calculated from rhyolites and migmatites[46] (Fig. 5); therefore, $D_{Li}^{Mineral/Melt}$ derived from natural samples should be used cautiously.

Experimental $D_{Li}^{Mineral/Melt}$ may also vary markedly as a function of experimental conditions, and its effect on the composition of minerals and melts (Fig. 5). Most notably, the $D_{Li}^{Pl/Melt}$ (0.48 ± 0.07) and $D_{Li}^{Afs/Melt}$ (0.2 ± 0.1) obtained in this study are over an order of magnitude higher than the partition coefficients that were previously used to model lithium enrichment during crustal anatexis (0.01–0.02)[13]. Low $D_{Li}^{Pl/Melt}$ and $D_{Li}^{Afs/Melt}$ are typically derived from pegmatites[49,50] or a single low-temperature crystallisation experimental study (600 °C)[23]. The comparatively high $D_{Li}^{Pl/Melt}$ from this study are consistent with the range of experimental partition coefficients obtained at magmatic conditions (>750 °C; Fig. 6a)[21] and with $D_{Li}^{Pl/Melt}$ derived from rhyolites or migmatites[10,44–48]. At first order, there is an observed temperature effect on the substitution of lithium into plagioclase in granitic systems. A similar temperature effect on the partitioning of lithium

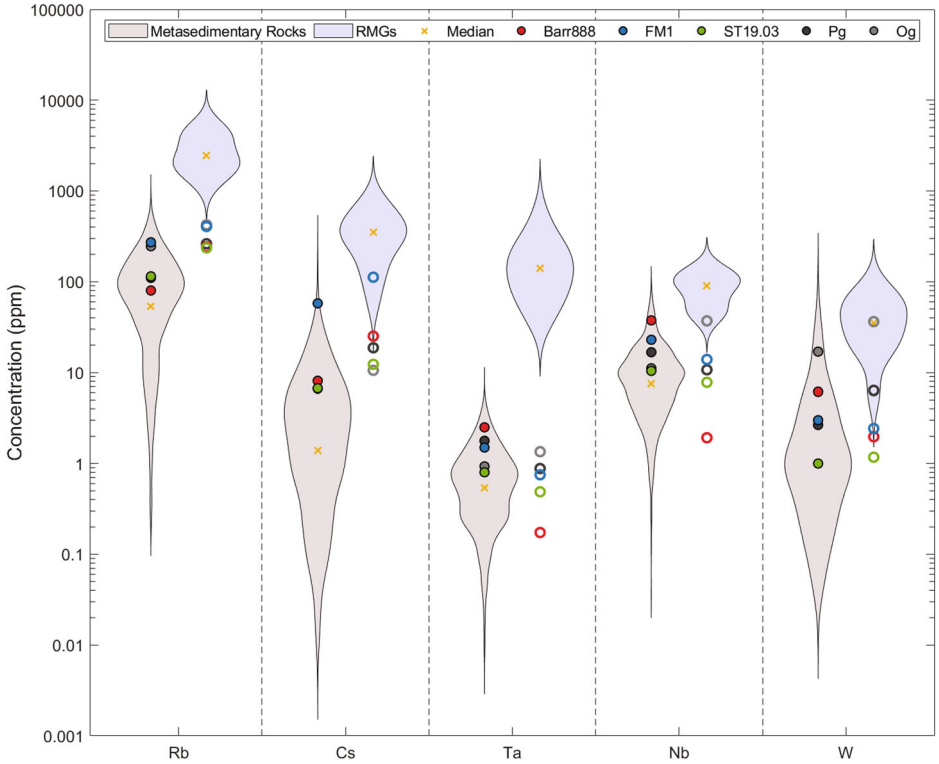

Fig. 4 | The mean rare metal content of the starting metasedimentary rocks (●) and glasses from the low-degree, fluid-absent partial melting experiments (○). Violin plots in grey and blue represent the distribution of rare metals in metasedimentary rocks ($n = 1481$; see Supplementary Data 2) and rare-metal granites ($n = 86$)[5], respectively. The 'Pg' and 'Og' experiments were derived from Michaud et al.[25]. Error bars, defined as the standard deviation of the mean ($1\sigma_m$), are smaller than the size of the symbols.

into alkali feldspar could not be identified (Fig. 6b); therefore, the reasons for the variation remain unclear. The $D_{Li}^{Afs/Melt}$ from this study are consistent with the partition coefficients calculated from the experiments of Maneta and Baker[18] and Sirbescu et al.[20], as well as $D_{Li}^{Afs/Melt}$ obtained from rhyolites and migmatites[44–48]. In contrast, $D_{Li}^{Afs/Melt}$ derived from granites and pegmatites[49,50] is up to an order of magnitude lower than the $D_{Li}^{Afs/Melt}$ observed in rhyolites and migmatites[44–48].

The $D_{Li}^{Bt/Melt}$ obtained in this study (0.5 ± 0.1) are consistent with previous experimental $D_{Li}^{Bt/Melt}$ (Fig. 5); however, they are lower than the partition coefficients used by Knoll et al.[11] and Koopmans et al.[13] for trace element modelling (1.6–1.7). The effect of temperature or mineral and melt compositions on $D_{Li}^{Bt/Melt}$ could not be identified due to the limited temperature range of biotite stability and the complex substitution mechanism of lithium into both lattice and interstitial sites in micas[47] (Fig. 6c). Nevertheless, the comparatively higher lithium content in staurolite relative to biotite is consistent with the partitioning behaviour of lithium between common metamorphic minerals. In micas, lithium substitutes into octahedral sites, whereas in staurolite, lithium partitions into energetically favourable tetrahedral sites[30]. Consequently, lithium preferentially partitions into staurolite over biotite[30], which is reflected by the higher $D_{Li}^{St/Melt}$ relative to $D_{Li}^{Bt/Melt}$ in the experimental run products. In natural rhyolitic samples, $D_{Li}^{Bt/Melt}$ is considered to be unusually high due to the entrapment of exsolved, lithium-rich fluids during the low-temperature crystallisation of micas[53,54]. In contrast, unaltered biotite that crystallised at high temperature (e.g., in phonolites) yields $D_{Li}^{Bt/Melt}$ that are consistent with experimental partition coefficients[53]. The lithium content of residual biotite and plagioclase is comparable in the experiments from this study, which is consistent with previous analyses in unaltered migmatites[44].

Experimental $D_{Li}^{Crd/Melt}$ from this study and from Evensen and London[17] are considerably lower than the partition coefficients derived from migmatites[10,44] (Fig. 5). The lithium content of cordierite is governed by the substitution of Li^+ for Mg^{2+} due to the similar ionic radii of the two cations[55]. Cordierite from migmatites is typically magnesium-poor (and iron-rich); therefore, it has a relatively high lithium content[10,44]. In comparison, newly crystallised cordierite from this study and from Evensen and London[17] is magnesium-rich and iron-poor. Consequently, the lithium content of experimental cordierite is relatively low compared to some natural samples. Similar to biotite, lithium preferentially partitions into staurolite over cordierite[30], which is consistent with the calculated $D_{Li}^{Mineral/Melt}$ in the experiments.

Partition coefficients of lithium in quartz also vary between natural and experimental samples. The lithium content of quartz is controlled by the coupled substitution[56] of Li^+ and Al^{3+} for Si^{4+}. The aluminium content of quartz in the experiments is considerably lower than in natural volcanic rocks[46–48], which likely reflects the slow diffusivity of aluminium at magmatic conditions. The diffusive modification of aluminium in quartz is considered to be negligible at 750 °C over several millions of years[56]. Therefore, residual crystals of quartz in anatectic regimes are depleted in aluminium and lithium, similar to their metamorphic source (Tables S6 and S7 in Supplementary Data 1). The $D_{Li}^{Quartz/Melt}$ obtained in this study are comparable to the partition coefficients calculated from the experiments of Maneta and Baker[18] and Pichavant[22]; therefore, they are considered to be representative of natural systems.

The newly constrained partition coefficients from this study demonstrate that lithium is not as incompatible in minerals as previously interpreted from $D_{Li}^{Mineral/Melt}$ derived from granitic rocks. Pegmatites form by low-temperature, disequilibrium crystallisation, during which trace elements may behave differently compared to high-temperature magmatic processes[51]. In contrast, partition coefficients derived from natural rhyolitic and migmatitic samples are likely overestimated due to the late-stage alteration of minerals (e.g., micas; Fig. 5) and glasses by hydrothermal fluids[53,54]. Therefore, lithium enrichment during crustal anatexis is likely overestimated or underestimated in trace element models using partition coefficients derived from granites[13] and rhyolites[48,57], respectively (Supplementary Fig. 6). To fully understand the variability of mineral-melt partition coefficients, it is imperative to further investigate the effect of experimental conditions and the composition of minerals and melts on the partitioning behaviour of lithium in felsic systems. At present, the existing and newly constrained $D_{Li}^{Mineral/Melt}$ should only be applied to systems that crystallised at conditions that are comparable to the experimental conditions in this study.

Table 3 | Representative major and trace element compositions of minerals in the FM1 experimental run products

Sample	$St_{(res)}$ GAR 01	$Bt_{(res)}$ GAR 01	$Grt_{(res)}$ GAR 01	$Crd_{(new)}$ GAR 03	$Tur_{(new)}$ GAR 01	$Pl_{(res)}$ GAR 01	$Afs_{(new)}$ GAR 01	$Qz_{(res)}$ GAR 01	$Hc_{(new)}$ GAR 15	$Mag_{(new)}$ GAR 03
wt%	*n* = 16	*n* = 8	*n* = 10	*n* = 6	*n* = 2	*n* = 4	*n* = 6	*n* = 4	*n* = 1	*n* = 3
SiO_2	27.4 (7)	38 (2)	36.0 (3)	48.9 (2)	36 (3)	67.6 (8)	64.6 (4)	100.7 (6)	0.25	0.13 (6)
TiO_2	0.5 (1)	1.6 (3)	0.05 (3)	b.d.[a] to 0.2	0.6 (1)	b.d. to 0.02	0.02 (1)	0.006	0.65	1.4 (5)
Al_2O_3	53.9 (9)	19.9 (4)	20.7 (1)	34.7 (5)	32 (2)	20.7 (6)	19.1 (8)	0.04 (3)	48.17	2.7 (3)
$FeO_{(t)}$	13 (1)	12 (1)	34 (2)	3.2 (6)	8 (2)	0.17 (6)	0.4 (1)	0.2 (1)	41.41	85.0 (6)
MgO	3 (1)	14.1 (9)	1.5 (3)	11.6 (1)	5.6 (2)	0.016 (7)	0.02 (1)	0.02 (2)	7.34	0.12 (3)
MnO	0.3 (2)	0.09 (6)	7 (2)	0.3 (1)	0.10 (3)	0.05 (3)	0.04 (2)	b.d.	1.50	0.03 (1)
CaO	0.04 (3)	b.d. to 0.02	1.1 (2)	0.09 (3)	0.8 (4)	1.6 (4)	0.4 (3)	b.d.	0.02	0.03 (1)
Na_2O	b.d. to 0.01	0.48 (9)	0.04 (4)	0.13 (6)	1.8 (2)	10.1 (4)	2.1 (7)	0.03	0.02	0.01
K_2O	0.06 (2)	9.3 (9)	0.012 (9)	0.15 (7)	b.d. to 0.04	0.5 (3)	13 (1)	0.013 (6)	0.05	0.11 (2)
ZnO	n.a.[b]	n.a.	0.06 (4)	0.04 (3)	n.a.	0.12	b.d.	0.06 (3)	n.a.	n.a.
P_2O_5	0.07 (6)	b.d. to 0.03	0.03 (3)	0.06 (4)	n.a.	0.13 (7)	0.06 (4)	0.03 (2)	0.04	0.03
F	b.d.	n.a.	b.d.	b.d.	n.a.	0.05 (4)	0.2 (1)	b.d.	n.a.	n.a.
Cl	0.02	n.a.	0.006 (5)	0.005 (2)	n.a.	0.007 (1)	0.007	0.0057 (9)	n.a.	n.a.
-(F,Cl) = O	0.004	n.a.	b.d. to 0.0005	b.d. to 0.0004	n.a.	b.d. to 0.02	0.09 (6)	0.0013 (2)	n.a.	n.a.
Total	99 (1)	95 (1)	100.3 (7)	99.3 (3)	85 (2)	101.0 (6)	100.0 (8)	101.0 (5)	99.45	89.5 (9)
ppm	***n* = 9**	***n* = 5**	***n* = 7**	***n* = 8**	***n* = 2**	***n* = 3**	***n* = 2**	***n* = 3**	***n* = 3**	***n* = 1**
Li	240 (40)	199 (6)	130 (20)	80 (20)	48 (9)	270 (30)	70 (30)	4.6 (3)	4.4 (7)	b.d.
Rb	5 (2)	790 (50)	0.24 (6)	20 (5)	n.a.	b.d. to 3.92	340 (30)	0.03 (2)	b.d.	b.d.
Nb	1.7 (3)	37 (2)	0.03 (2)	b.d. to 0.07	0.14 (7)	0.12	0.6 (6)	0.0005	0.38 (5)	135
Cs	1.1 (5)	260 (80)	b.d.	23 (4)	n.a.	b.d. to 0.59	10 (7)	0.011 (2)	0.1	b.d.
Ta	0.24 (6)	2.0 (2)	0.03 (1)	0.011 (3)	0.017 (6)	b.d.	0.02 (1)	0.0008	0.02 (1)	5.51
W	0.05 (5)	0.7 (3)	0.04 (2)	0.06	b.d.	b.d.	0.2 (1)	0.006	b.d.	43.13
D_{Li}[c]	0.51 (9)	0.42 (1)	0.28 (5)	0.29 (8)	0.10 (2)	0.58 (6)	0.14 (6)	0.0098 (6)	0.022 (3)	b.d.
D_{Rb}	0.010 (4)	1.8 (1)	0.0006 (1)	0.06 (2)	b.d.	b.d. to 0.009	0.79 (8)	0.00006 (4)	b.d.	b.d.
D_{Nb}	0.12 (2)	2.8 (2)	0.002 (1)	b.d. to 0.009	0.011 (5)	0.009	0.04 (4)	0.00004	0.070 (9)	17.25
D_{Cs}	0.009 (4)	2.0 (6)	b.d.	0.34 (6)	b.d.	b.d. to 0.004	0.08 (6)	0.00008 (2)	0.001	b.d.
D_{Ta}	0.32 (8)	2.7 (2)	0.03 (1)	0.025 (6)	0.022 (8)	b.d.	0.03	0.001	0.04 (2)	12.33
D_W	0.02 (2)	0.3 (1)	0.015 (7)	0.01	b.d.	b.d.	0.09	0.003	b.d.	6.57

Mineral abbreviations are given in Fig. 3. Detailed major and trace element compositions of minerals in the starting materials and experimental run products are reported in Tables S6–S11 in Supplementary Data 1. Uncertainty is reported to the last digit(s) in the brackets as the standard deviation of the mean ($1\sigma_m$). '*n*' denotes the number of analyses.

[a]b.d. = below detection.

[b]n.a. = not analysed.

[c]Partition coefficients are calculated using Eq. (5).

Discussion

The lithium content of partial melts is a complex function of the metasedimentary source composition, the melting reactions, the degree of melting, and the partitioning of rare metals between minerals and melts. The enrichment of lithium is maximised during the low-degree partial melting of lithium-rich metasedimentary rocks and the complete breakdown of staurolite, which can remain stable up to 700–855 °C[11,35,58–60]. To further constrain lithium enrichment in such anatectic regimes, the partial melting of crustal rocks was modelled.

The model was first used to quantify the enrichment of lithium in the experiments from this study, the partial melting experiments of Michaud et al.[25], and the crystallisation experiments of Pichavant[22] (Fig. 7a and b). The calculations were constrained using the mean $D_{\mathrm{Li}}^{\mathrm{Mineral/Melt}}$ from this study and the modal mineralogy of the run products (Supplementary Fig. 3; Tables S3 and S12 in Supplementary Data 1). Partition coefficients of corundum and sillimanite could not be determined due to the small size of these crystals (e.g., Fig. 3); therefore, $D_{\mathrm{Li}}^{\mathrm{Als/Melt}}$ and $D_{\mathrm{Li}}^{\mathrm{Crn/Melt}}$ were fixed to 0.01, based on the analyses of matrix glasses and phenocrysts in natural rhyolitic samples[48]. Bulk partition coefficients of lithium ($\bar{D}_{\mathrm{Li}}$) were determined according to the equation:

$$\bar{D}_{\mathrm{Li}} = \sum_{i=0}^{n} D_{\mathrm{Li}}^{\mathrm{Mineral/Melt}} \times X_i^{\mathrm{Mineral}}, \tag{6}$$

where X_i^{Mineral} is the modal proportion of a phase in the assemblage. Bulk partition coefficients are comparable between fluid-absent melting, fluid-present melting, and crystallisation experiments of all starting materials. The $\bar{D}_{Li}$ of the experiments varies between 0.12 and 0.22 (Table 2 and Table S8 in Supplementary Data 1), which demonstrates that lithium is moderately incompatible in the minerals of the run products. Crustal anatexis was modelled using a modal batch melting model[42]:

$$C_{Melt} = \frac{C_{Bulk}}{F\left(1 - \bar{D}_{Li}\right) + \bar{D}_{\mathrm{Li}}}, \tag{7}$$

where C_{Melt} is the lithium content in the melt, C_{Bulk} is the bulk lithium content in the metasedimentary rocks, and F is the fraction of melt produced. The modelled and experimental results are in good agreement (Fig. 7a and b), which corroborates the applicability of the newly constrained partition coefficients and verifies that all lithium-bearing phases were accounted for in the experiments.

The model was subsequently used to simulate the partial melting of crustal rocks with variable lithium contents (Fig. 7c). The degree of melting was limited to 7–30%, comparable to previous numerical models[10,11,13]. First, the anatexis of conventional metasedimentary rocks (20 ppm lithium) and the subsequent magmatic differentiation of the partial melts were modelled to demonstrate the petrogenesis of common lithium-poor peraluminous granites in the crust (<100 ppm lithium; Supplementary Discussion and Supplementary Fig. 7). Then, the partial melting of enriched crustal rocks was investigated to constrain the anatectic source of RMGPs. Two crustal rocks were considered, including the staurolite-bearing micaschist from Knoll et al.[11] ('RS34/01'; 269 ppm lithium) and the anatectic granite from Koopmans et al.[13] ('Granite–Greywacke source'; 538 ppm lithium). The lithium content of the anatectic granite is comparable to the highest recorded lithium content in metapelites and gneisses observed in nature (see Supplementary Data 2). The partial melting of the mean (1000 ppm lithium) and most enriched units (2290 ppm lithium) of an unconventional metabauxite was also considered ('Mb')[61]. Such lithologies are representative of metasedimentary rocks that may form by the metamorphism of lithium-rich bauxites, clays, or volcano-sedimentary deposits[26–28]. The model was constrained using the range of $\bar{D}_{\mathrm{Li}}$ determined from all fluid-absent melting experiments in this study, assuming a fixed modal mineralogy, the stability

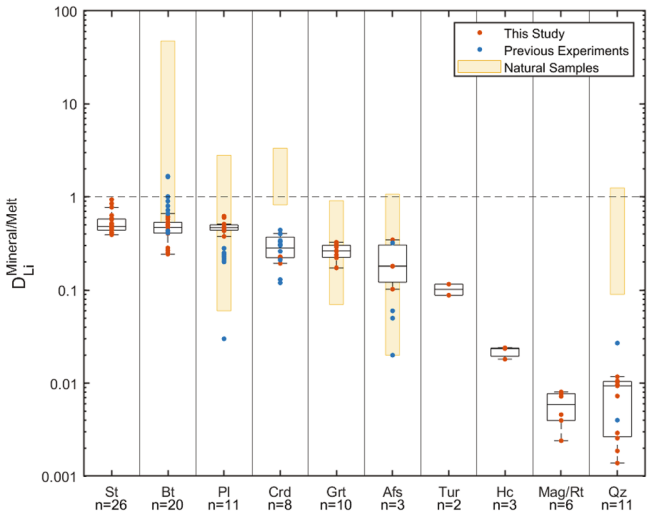

Fig. 5 | Mineral-melt partition coefficients of lithium obtained from the partial melting and crystallisation experiments (red circles and box plots). The range of partition coefficients from natural samples[10,44–48] and from previous experimental studies in felsic systems[16–23] are indicated by the orange box and the blue circles, respectively. The box plots highlight the median (centre line), upper and lower quartiles (box limits), and the maximum and minimum values within 1.5× the interquartile range (whiskers) from the experimental partition coefficients obtained in this study. Mineral abbreviations are reported in Fig. 3. '*n*' denotes the number of analyses.

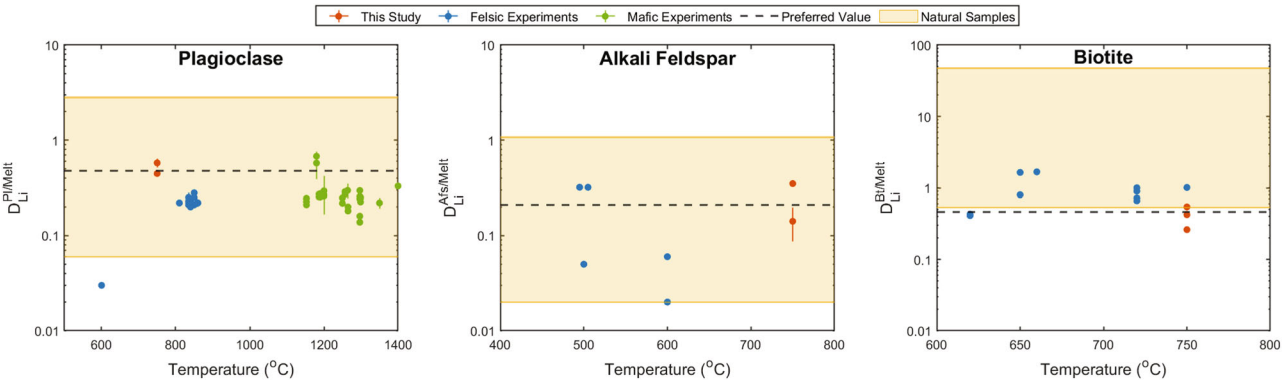

Fig. 6 | The effect of temperature on the partitioning of lithium into residual and newly crystallising minerals. a Plagioclase. **b** Alkali feldspar. **c** Biotite. Partition coefficients are presented from this study (red circles), felsic experiments in the literature[16,18–23] (blue circles), mafic experiments in the literature (green circles; Table S14 in Supplementary Data 1; Supplementary References), and natural samples[10,44–48] (range shown by the orange box). The dashed line highlights the preferred values that were subsequently used for trace element modelling. The error bars represent the standard deviation of the mean ($1\sigma_{\mathrm{m}}$).

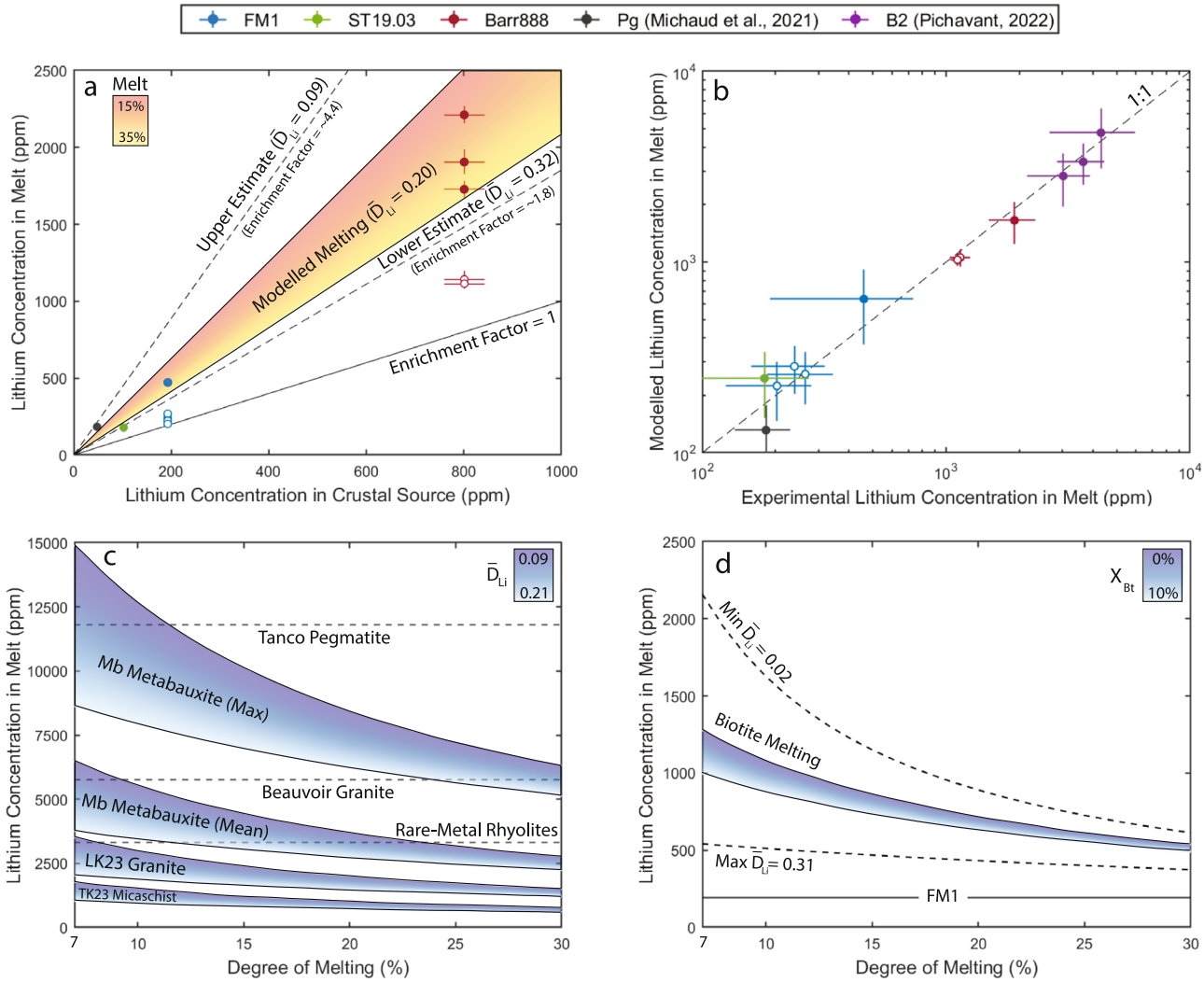

Fig. 7 | The enrichment of lithium during crustal anatexis. a The enrichment of lithium in the partial melts of the experiments from this study and the 'Pg' experiment of Michaud et al.[25]. Filled circles represent fluid-absent melting experiments, whereas open circles represent glasses from crystallisation, fluid-present, or high-temperature experiments. The modelled, lower, and upper estimates of lithium enrichment were calculated using the mean, minimum, and maximum values of partition coefficients, respectively, and the modal mineralogy of the fluid-absent melting experiments. **b** Comparison of the experimental and modelled lithium contents in partial melts. The error bars represent the standard deviation of the mean ($1\sigma_m$). **c** The enrichment of lithium during the partial melting of crustal rocks of diverse compositions, taken from Franceschelli et al. ('Mb'; 1000 and 2290 ppm lithium)[61], Knoll et al. ('RS34/01'; 229 ppm lithium)[11], and Koopmans et al. ('Granite–Greywacke source'; 538 ppm lithium)[13]. **d** Sensitivity test of the trace element model to highlight the effect of biotite breakdown during the anatexis of the FM1 micaschist. The effect of using variable $D_{Li}^{Mineral/Melt}$ from previous experimental studies is demonstrated by the dashed lines.

or metastability of staurolite during the onset of partial melting, and the subsequent breakdown of staurolite and biotite during anatexis ($\bar{D}_{Li}$ = 0.09 to 0.21; Table S13 in Supplementary Data 1). The partial breakdown of biotite was also investigated (Fig. 7d), which has a marked effect on the enrichment of lithium, as well as other rare metals such as Rb, Cs, W, Nb, and Ta (Supplementary Discussion and Supplementary Fig. 8).

Lithium may become enriched in the partial melts by up to a factor of 5–6 during the low-degree (<10%) dehydration-melting of staurolite and biotite (Fig. 7c). The anatexis of the RS34/01 micaschist produces a partial melt with up to ~1500 ppm lithium (Fig. 7c), which is comparable to weakly enriched RMGPs (Fig. 1b). The low-degree partial melting of the anatectic granite forms a melt with a lithium content that is consistent with the mean composition of RMGPs and rare-metal rhyolites (~3000 ppm lithium). The partial melts produced by the anatexis of the micaschist and the granite must become further enriched by moderate fractional crystallisation[48,57] or the re-melting of granitic cumulates[13] to produce high-grade RMGP deposits (>5000 ppm lithium). Assuming that the partitioning behaviour of lithium is similar during anatexis and fractionation, it is estimated that the parental melts of highly fractionated RMGPs and rare-metal rhyolites (>3000 ppm lithium, ~75% fractional crystallisation) must contain at least 1000 ppm lithium (Fig. 7c). These modelled results are consistent with high-grade granite-related deposits being sourced from enriched crustal rocks.

An alternative hypothesis to this petrogenetic model is the formation of potential RMGPs by the anatexis of unconventional metasedimentary rocks (>1000 ppm lithium). The partial melting of the mean and most enriched units of the Mb metabauxite may produce a melt with up to ~6500 and ~14,000 ppm lithium, respectively. Other rare metals (Rb, Cs, Ta) and major elements (Na_2O, P_2O_5, and F) can become further enriched during the moderate fractional crystallisation of extracted melts (<75%)[48,57] or late-stage metasomatic processes[40]. The magmatic differentiation and subsequent emplacement of undercooled melts in the upper crust can further reconcile the geochemical and textural features of pegmatites[4]. To test

whether RMGPs are sourced from unconventional deposits, it is important to constrain the occurrence and size of enriched metasedimentary rocks in nature. There are several known examples of bauxites or low-grade metabauxites at active continental margins, which may contain up to 8200 ppm lithium[28,62]. However, the high-grade equivalents of these deposits are poorly explored in orogenic settings due to their low preservation potential and small volume. Lithium-rich metabauxites are typically found as thin lenses (~1–15 m) within carbonate rocks that extend for up to a few hundred metres in length[61,62]. The anatexis of interlayered bauxite and carbonate units can produce weakly peraluminous felsic melts[63]; however, the Al_2O_3 and K_2O content of glasses produced by such experiments is enriched relative to RMGPs or glasses produced by the anatexis of metapelites. Furthermore, the partial melting of thin lenses of metabauxites (<1 km^3) would produce small-volume potential pegmatite-forming melts. However, in order to produce a Beauvoir-like granite (~1 km^3 and ~5800 ppm lithium) by low-degree anatexis (<10%), ~10 km^3 of a lithium-rich (~1000 ppm) metasedimentary sequence must be melted (Fig. 7c). The erosion of bauxites and their subsequent deposition in sedimentary sequences[28] may form such voluminous pelitic rocks that can source RMGPs. Alternatively, the metamorphism of lithium-rich clays (up to 2400 ppm)[2], tuffaceous sedimentary rocks (up to 4160 ppm)[57], or Jadar-type deposits (8400 ppm)[2] may also produce extensive metapelitic or metavolcanic sequences containing >1000 ppm lithium following metamorphic devolatilisation. Although metapelites became widespread by the late Archean (2.8–2.5 Ga)[64], it is unlikely that such rocks could have sourced the oldest RMGPs observed in nature (~3 Ga)[12] due to the scarcity of highly aluminous metapelites in the Mesoarchean[4]. In contrast, paragneisses and orthogneisses metasomatised by volatile-rich mantle-derived granitoids (sanukitoids) are abundant in Archean terranes; therefore, they are inferred to be important sources of several Precambrian RMGPs[65,66]. Paragneisses in particular can have a notably high lithium content (up to 560 ppm), which is comparable to metapelitic rocks observed in diverse geological settings (up to 600 ppm lithium; see Supplementary Data 2). However, unconventional metapelites, gneisses, and metavolcanic rocks containing >1000 ppm lithium have not yet been identified in nature. Therefore, it is imperative to improve exploration prospects for such lithologies to test whether they can source RMGPs. The complex structural, temporal, and spatial variability of sedimentary rocks, metamorphic rocks, and RMGPs in nature makes it challenging to establish a link between pegmatites and their crustal source. Partial melts sourced from metasedimentary rocks must get extracted and transported several kilometres through the crust before getting emplaced in host rocks that facilitate undercooling[9]. Thus, lithium-rich sedimentary rocks that are Cenozoic in age do not provide an accurate representation of the crustal rocks that source Precambrian or Palaeozoic RMGPs that are found in nature[12]. Therefore, it is critical to better constrain the redistribution of lithium during metamorphism in order to interpret the lithium content of metasedimentary rocks that are sourced from enriched sedimentary protoliths.

Conclusions

In conclusion, lithium enrichment in RMGPs begins with the anatexis of an enriched crustal source (>300 ppm lithium). The metamorphism of lithium-rich sedimentary deposits may produce unconventional metasedimentary rocks (>1000 ppm lithium), which can undergo anatexis to produce potential pegmatite-forming melts, containing >5000 ppm lithium. Other rare metals (Rb, Cs, and Ta) and major elements (Na_2O, P_2O_5, and F) can become further enriched during the fractional crystallisation of extracted melts or late-stage metasomatic processes. Alternatively, high-grade RMGPs (>5000 ppm lithium) may form by the low-degree (~10%) partial melting of enriched crustal rocks observed in nature (~300–600 ppm lithium), followed by the moderate fractional crystallisation (<75%) of the extracted melts or the re-melting of granitic cumulates. Lithium-rich metasedimentary rocks (>300 ppm lithium) are poorly explored in nature; therefore, it is important to further investigate their occurrence to better constrain the sources of RMGPs.

Methods

Experimental setup

The experiments were conducted in either a piston-cylinder apparatus or an internally heated pressure vessel at the Institute des Sciences de la Terre d'Orléans (ISTO), France (CNRS, BRGM, Université d'Orléans) (Table 1). To prepare the starting materials, the metasedimentary samples were powdered or melted at 1200 °C. Partial melting and crystallisation experiments were performed on rock powders and glasses, respectively, at 750–800 °C and 400–1000 MPa. The pressure–temperature conditions were chosen to investigate the dehydration melting of white micas and staurolite in orogenic settings[25,35,36,58–60]. Water was added to some of the charges to investigate the melting of biotite (Table 1).

The starting materials (~200 g) were crushed and ground using an agate mortar until the minerals were finely powdered (<10 μm). The powders (30–50 mg) were loaded in 5 mm outer diameter gold capsules for the partial melting experiments, and Au–Pd (80% gold, 20% palladium) capsules for the crystallisation and high-temperature experiments. Water was subsequently added to the fluid-present experiments (3–5 ml, equivalent to 10 wt%), and the capsules were welded shut.

The high-temperature melting experiments were performed in an internally heated pressure vessel at 1200 °C (±0.1 °C) and 200–400 MPa (±0.1 MPa)[67]. The vessel was pressurised with pure argon and 20 MPa of an Ar–H_2 gas mixture (2% volume hydrogen) in order to buffer the oxygen fugacity (f_{O_2}) of the system, which is calculated to be ~QFM. The apparatus was heated to 1200 °C, which was monitored using a K-type thermocouple. After 72 h, the samples were quenched using a drop-quench mechanism. At the start of the experiments, the capsules were placed in an alumina basket, which was suspended near the hot end of the vessel with a platinum wire. At the end of the experiments, the wire was cut by a current, and the alumina basket with the capsules fell down to the cold end of the vessel. The Barr888 glass was extracted, crushed, and reloaded into Au–Pd capsules for the crystallisation experiments (Table 1). The low-temperature partial melting and crystallisation experiments of Barr888 were subsequently performed in an internally heated pressure vessel at 800 °C, 400 MPa, and an f_{O_2} of ~QFM (20 MPa of Ar–H_2). At the end of the experiments (up to 120 h), the power to the vessels was cut, and the samples were quenched within ~5 min by the cooling system.

Low-temperature partial melting and crystallisation experiments of the three metasedimentary rocks were also performed in a Bristol-type piston-cylinder apparatus[37,68] using ¾ inch assemblies. The capsules were wrapped in an MgO sleeve, and the empty space was filled with MgO powder. The sleeve was placed in a graphite-Pyrex-talc assemblage. The piston-cylinder was over-pressurised and heated to the desired temperature (monitored using a B-type thermocouple). The FM1 and ST19.03 partial melting and crystallisation experiments were conducted at 750 °C (±0.1 °C) and 700 MPa (±1 MPa). In the crystallisation experiments, the samples were first melted at 1150 °C for ~24 h, then the apparatus was cooled down to 750 °C. The Barr888 low-temperature partial melting and crystallisation experiments were performed at 750–800 °C and 700–1000 MPa. High-temperature melting experiments were also performed on the metabauxite at 1000–1200 °C and 700–1000 MPa. The oxygen fugacity in the Barr888 experiments was buffered at CCO by the presence of carbon (ankerite) and sulfur (pyrite) in the metabauxite[37]. In contrast, the oxygen fugacity of the FM1 and ST19.03 experiments evolved from intrinsic (CCO)[37] to increasingly oxidising conditions following the dissociation of water to H_2, and the diffusion of hydrogen through the capsule walls[37]. The piston-cylinder experiments lasted between 48 and 430 h. At the end of the experiments, power to the apparatus was cut, and the samples were rapidly quenched within <1 min by the cooling system. After the quenching, the capsules were cut in half, mounted in a 1-inch ring mount, and the samples were polished.

Scanning electron microscopy (SEM)

All analyses of the starting materials and the run products were carried out at ISTO-CNRS-BRGM. The imaging of the samples and the identification of minerals were performed using a Merlin compact ZEISS scanning electron

microscope[67]. Imaging was performed by backscattered electron imaging, and minerals were identified using a Bruker QUANTAX-Xflash6 energy-dispersive spectrometer. The analyses were conducted using a focused beam with an accelerating voltage of 15 kV and a diaphragm diameter of 60 µm.

Electron probe microanalysis (EPMA)

Major element analyses were conducted using a CAMECA SX-Five or a JEOL IHP 200F electron probe microanalyser[67]. Analyses were performed using a defocused beam, with a diameter of 1–20 µm for minerals and 10–20 µm for glasses in order to limit the diffusion of alkalis. The accelerating voltage and intensity of the electron beam were 15 kV and 5–6 nA, respectively. Major elements were quantified by wavelength-dispersive spectroscopy. Sodium and potassium were analysed first in order to limit their diffusion under the electron beam. The conditions, standards, and crystals used for the analyses of both microprobes are summarised in Table S1 in Supplementary Data 1. All analyses are reported in Supplementary Data 3.

Laser ablation inductively coupled plasma mass spectrometry (LA-ICP-MS)

Trace element analyses were performed using a RESOlution-SE 193 nm Ar–F excimer laser ablation system with a Laurin Technique S155 ablation cell coupled with an Agilent 8900 QQQ quadrupole mass spectrometer[67]. A detailed description of the system parameters is summarised in Table S2 in Supplementary Data 1. The fluence and repetition rate of the beam were varied according to the phase analysed. Glasses were analysed at 2 J/cm^2 and 5 Hz, micas at 4–5 J/cm^2 and 5 Hz, other ferromagnesian minerals (staurolite, garnet, cordierite, and tourmaline) at 5 J/cm^2 and 5 Hz, oxides at 4 J/cm^2 and 3 Hz, feldspars at 4 J/cm^2 and 5 Hz, and quartz at 5–7 J/cm^2 and 5 Hz. All analyses were performed with a SQUID to smooth out signals at the low repetition rates. The beam diameter was kept constant at 10–20 µm. The trace element composition of phases could not be determined in some experiments due to the small size of melt pockets and crystals (<10 µm). The analysed isotopes include ^{7}Li, ^{9}Be, ^{11}B, ^{23}Na, ^{24}Mg, ^{27}Al, ^{29}Si, ^{31}P, ^{35}Cl, ^{39}K, ^{44}Ca, ^{47}Ti, ^{51}V, ^{53}Cr, ^{55}Mn, ^{56}Fe, ^{59}Co, ^{60}Ni, ^{63}Cu, ^{66}Zn, ^{71}Ga, ^{72}Ge, ^{85}Rb, ^{88}Sr, ^{89}Y, ^{90}Zr, ^{93}Nb, ^{115}In, ^{118}Sn, ^{133}Cs, ^{137}Ba, ^{139}La, ^{140}Ce, ^{141}Pr, ^{146}Nd, ^{147}Sm, ^{153}Eu, ^{157}Gd, ^{172}Yb, ^{178}Hf, ^{181}Ta, ^{182}W, ^{208}Pb, ^{232}Th, and ^{238}U. The isotopes were each measured at a dwell time of 10 ms, with a total sweep time of 0.4–0.7 s. The instrument settings were tuned following the ablation of a NIST-612 standard in order to minimise isotope fractionation (U/Th = 1.00 ± 0.02%), the production of oxides (ThO/Th < 0.1%), and the production of doubly charged ions ($^{42}Ca^{2+}/^{42}Ca^{+}$ < 0.2%). A NIST-610 glass was used as the external standard, and NIST-612 and BCR-2G glasses were used as standards for quality control in silicate minerals. For the oxides, a GSE-2G glass was used as the external standard, and GSD-2G as a standard for quality control. Three analyses were performed on the external standards, and 1 analysis was performed on the quality control standards after every 10–15 analyses of the samples. The raw data were processed with Glitter[69] using a linear fit to correct for instrument drift. To quantify the trace elements, SiO_2 and FeO or TiO_2 were used as the internal standards for silicate minerals and Fe-Ti oxides, respectively. The signals were individually screened to identify contaminated analyses. Time-resolved signals that showed element spikes or irregular shapes resulting from the analyses of mixed phases were discarded (Supplementary Fig. 1). The precision and accuracy of lithium analyses in the quality control reference materials (NIST-612, BCR-2g, and GSD-2G) were mostly better than 2%, 5%, and 15%, respectively (see Supplementary Data 4).

Bulk composition

The bulk composition of all three starting materials was determined by major (EPMA) and trace element (LA-ICP-MS) analyses of the homogeneous glasses produced by the high-temperature (1200 °C) melting experiments in an internally heated pressure vessel at ISTO-CNRS-BRGM (Table 1). The starting materials used for the high-temperature and low-temperature partial melting experiments were derived from the same rock powders to ensure that bulk rock analyses are representative. Minor traces of sillimanite and corundum are present as evenly distributed residual phases in the Barr888 high-temperature experiment (A1); therefore, major and trace element analyses were performed with a beam size of 100 µm on clusters of glass, corundum, and sillimanite.

Modal mineralogy

The modal proportion of phases in the metasedimentary rocks and the run products was determined by mass balance calculations (Supplementary Fig. 3) due to the heterogeneous nature of the samples. A linear least-squares regression fit was applied to the normalised major element composition of the assemblages (minerals, glasses, and bulk rock) using the *lsqlin* function in MATLAB[24]. In the calculations, it is assumed that the bulk composition of the sample remains constant before and after the experiments. The modal mineralogy of the starting materials and the run products, as well as the uncertainty associated with the calculations, is reported in Tables S3 and S4 in Supplementary Data 1, respectively. Phase proportions could only be determined for some of the experiments because the minerals were too small to be analysed in several samples using an electron microprobe.

Trace element modelling

The anatectic model was constrained using the experiments from this study, partial melting experiments on a paragneiss ('Pg') by Michaud et al.[25], and the crystallisation experiments on the Beauvoir granite by Pichavant[22] (Fig. 7a and b). The modal mineralogy of the Pg experiment (6% biotite, 35% plagioclase, 9% alkali feldspar, 42% quartz, 5% orthopyroxene, 4% spinel) was calculated using the modal abundance of minerals in the paragneiss and the stoichiometry of the melting reactions established in Michaud et al.[25]. Partition coefficients of orthopyroxene (0.2) were derived from Neukampf et al.[46]. The modal mineralogy of the Beauvoir crystallisation experiments was taken from Pichavant[22]. Michaud et al.[25] have also performed partial melting experiments on an orthogneiss ('Og'); however, these were not considered for the trace element modelling of lithium due to underestimations of the bulk lithium and caesium contents by mass balance calculations[25].

The anatexis of variably enriched crustal rocks in nature (Fig. 7c) was modelled using the mean $D_{Li}^{Mineral/Melt}$ obtained from all experiments in this study. The sensitivity of the model was tested using variable $D_{Li}^{Mineral/Melt}$ derived from previous experimental studies[16–23], rhyolites[48], and granites[13]. The use of variable partition coefficients can yield a wide range of $\bar{D}_{Li}$ values (0.02–0.31), which can lead to strikingly different interpretations of lithium endowment during crustal anatexis. For example, at low melt fractions (~10%), the enrichment of lithium during the complete breakdown of biotite may vary between a factor of ~2.5 and ~10 as a function of $\bar{D}_{Li}$ calculated from previous experiments (Fig. 7d) or natural rhyolitic and granitic samples (Supplementary Fig. 6).

Reporting summary

Further information on research design is available in the Nature Portfolio Reporting Summary linked to this article.

Data availability

The authors declare that the data supporting the findings of this study are available within the paper and its supplementary files. The Supplementary Data are also available on Recherche Data Gouv, at https://doi.org/10.57745/UILJWI.

Received: 12 May 2025; Accepted: 16 October 2025;
Published online: 26 November 2025

References

1. Clemens, J. D. & Stevens, G. What controls chemical variation in granitic magmas?. *Lithos* **134–135**, 317–329 (2012).

2. Bowell, R. J., Lagos, L., de los Hoyos, C. R. & Declercq, J. Classification and characteristics of natural lithium resources. *Elements* **16**, 259–264 (2020).
3. Cameron, E. N., Jahns, R. H., McNair, A. H. & Page, L. R. Internal structure of granitic pegmatites. In *Economic Geology Monograph* Vol. 2 (eds Cameron, E. N., Jahns, R. H., McNair, A. H. & Page, L. R.) 1–112 (Society of Economic Geologists, 1949).
4. Černý, P., Blevin, P. L., Cuney, M. & London, D. Granite-related ore deposits. In *One-Hundredth Anniversary Volume: Economic* Geology (eds Hedenquist, J. W., Thompson, J. F. H., Goldfarb, R. J. & Richards, J. P.) 337–370 (Society of Economic Geologists, 2005).
5. Linnen, R. L. & Cuney, M. Granite-related rare-element deposits and experimental constraints on Ta–Nb–W–Sn–Zr–Hf mineralization. In *Rare-Element Geochemistry and Mineral Deposits* (eds Linnen, R. L. & Samson, I. M.) 45–68 (Geological Association of Canada Short Course Notes 17, 2005).
6. Stewart, D. B. Petrogenesis of lithium-rich pegmatites. *Am. Mineral.* **63**, 970–980 (1978).
7. Simmons, W. et al. Bulk composition of Mt. Mica Pegmatite, Maine, USA: implications for the origin of an LCT type pegmatite by anatexis. *Can. Mineral.* **54**, 1053–1070 (2016).
8. Müller, A., Romer, R. L. & Pedersen, R. B. The Sveconorwegian pegmatite province—thousands of pegmatites without parental granites. *Can. Mineral.* **55**, 283–315 (2017).
9. Plunder, A. et al. Pegmatites as geological expressions of spontaneous crustal flow localisation. *Lithos* **416–417**, 1–13 (2022).
10. Ballouard, C. et al. A felsic meta-igneous source for Li-F-rich peraluminous granites: insights from the Variscan Velay dome (French Massif Central) and implications for rare-metal magmatism. *Contrib. Mineral. Petrol.* **178**, 1–24 (2023).
11. Knoll, T. et al. Lithium pegmatite of anatectic origin—a case study from the Austroalpine Unit Pegmatite Province (Eastern European Alps): geological data and geochemical modelling. *Ore Geol. Rev.* **154**, 1–32 (2023).
12. Gardiner, N. J., Palin, R. M., Koopmans, L., Mangler, M. F. & Robb, L. J. On tin and lithium granite systems: a crustal evolution perspective. *Earth-Sci. Rev.* **258**, 1–23 (2024).
13. Koopmans, L. et al. The formation of lithium-rich pegmatites through multi-stage melting. *Geology* **52**, 7–11 (2024).
14. Vigneresse, J. L., Barbey, P. & Cuney, M. Rheological transitions during partial melting and crystallization with application to felsic magma segregation and transfer. *J. Petrol.* **37**, 1579–1600 (1996).
15. Dufek, J. & Bachmann, O. Quantum magmatism: magmatic compositional gaps generated by melt-crystal dynamics. *Geology* **38**, 687–690 (2010).
16. Icenhower, J. & London, D. An experimental study of element partitioning among biotite, muscovite, and coexisting peraluminous silicic melt at 200 MPa (H_2O). *Am. Mineral.* **80**, 1229–1251 (1995).
17. Evensen, J. M. & London, D. Experimental partitioning of Be, Cs, and other trace elements between cordierite and felsic melt, and the chemical signature of S-type granite. *Contrib. Mineral. Petrol.* **144**, 739–757 (2003).
18. Maneta, V. & Baker, D. R. Exploring the effect of lithium on pegmatitic textures: an experimental study. *Am. Mineral.* **99**, 1383–1403 (2014).
19. Pichavant, M., Villaros, A., Deveaud, S., Scaillet, B. & Lahlafi, M. The influence of redox state on mica crystallisation in leucogranitic and pegmatitic liquids. *Can. Mineral.* **54**, 559–581 (2016).
20. Sirbescu, M. L. C., Schmidt, C., Veksler, I. V., Whittington, A. G. & Wilke, M. Experimental crystallisation of undercooled felsic liquids: generation of pegmatitic texture. *J. Petrol.* **58**, 539–568 (2017).
21. Iveson, A. A., Rowe, M. C., Webster, J. D. & Neill, O. K. Amphibole-, clinopyroxene- and plagioclase-melt partitioning of trace and economic metals in halogen-bearing rhyodacitic melts. *J. Petrol.* **59**, 1579–1604 (2018).
22. Pichavant, M. Experimental crystallisation of the Beauvoir granite as a model for the evolution of Variscan rare metal magmas. *J. Petrol.* **63**, 1–28 (2022).
23. Gao, X. et al. Trace element (Be, Zn, Ga, Rb, Nb, Cs, Ta, W) partitioning between mica and Li-rich granitic melt: experimental approach and implications for W mineralization. *Geochim. Cosmochim. Acta* **375**, 1–18 (2024).
24. Gion, A. M., Piccoli, P. M., Fei, Y., Candela, P. A. & Ash, R. D. Experimental constraints on the formation of pegmatite-forming melts by anatexis of amphibolite: a case study from Evje-Iveland, Norway. *Lithos* **398–399**, 2–27 (2021).
25. Michaud, J. A. S., Pichavant, M. & Villaros, A. Rare elements enrichment in crustal peraluminous magmas: insights from partial melting experiments. *Contrib. Mineral. Petrol.* **176**, 1–33 (2021).
26. Kesler, S. et al. Global lithium resources: relative importance of pegmatite, brine and other deposits. *Ore Geol. Rev.* **48**, 55–69 (2012).
27. Balaram, V., Santosh, M., Satyanarayanan, M., Srinivas, N. & Gupta, H. Lithium: a review of applications, occurrence, exploration, extraction, recycling, analysis, and environmental impact. *Geosci. Front.* **15**, 1–47 (2024).
28. Wu, Z. Advance review on occurrence state and leaching of lithium in sedimentary bauxite (aluminum) deposits, China. *Ore Geol. Rev.* **164**, 1–11 (2024).
29. Gloaguen, É., Melleton, J., Gourcerol, B. & Millot, R. Lithium mineralization, contributions of paleoclimates and orogens. In *Metallic Resources* Vol. 2 (ed. Decrée, S.) 1–61 (Wiley-ISTE, 2023).
30. Dutrow, B. L., Holdaway, M. J. & Hinton, R. W. Lithium in staurolite and its petrologic significance. *Contrib. Mineral. Petrol.* **94**, 496–506 (1986).
31. Pattison, D. R. M. & Spear, F. S. Kinetic control of staurolite–Al_2SiO_5 mineral assemblages: implications for Barrovian and Buchan metamorphism. *J. Metamorph. Geol.* **36**, 667–690 (2018).
32. Raimbault, L. & Burnol, L. The Richemont rhyolite dyke, Massif Central, France: a subvolcanic equivalent of rare-metal granites. *Can. Mineral.* **36**, 265–282 (1998).
33. Gloaguen, É. Apports d'une étude intégrée sur les relations entre granites et minéralisations filoniennes (Au et Sn–W) en contexte tardiorogénique (Chaîne Hercynienne, Galice centrale, Espagne). Doctoral Thesis, Université d'Orléans, 1–572 (2006).
34. Chopin, C., Goffé, B., Ungaretti, L. & Obertie, R. Magnesiostaurolite and zincostaurolite: mineral description with petrogenetic and crystal-chemical update. *Eur. J. Mineral.* **15**, 167–176 (2003).
35. Patiño Douce, A. E. & Harris, N. Experimental constraints on Himalayan anatexis. *J. Petrol.* **39**, 689–710 (1998).
36. Patiño Douce, A. E. & Johnston, A. D. Phase equilibria and melt productivity in the pelitic system: implications for the origin of peraluminous granitoids and aluminous granulites. *Contrib. Mineral. Petrol.* **107**, 202–218 (1991).
37. Matjuschkin, V., Brooker, R. A., Tattitch, B., Blundy, J. D. & Stamper, C. C. Control and monitoring of oxygen fugacity in piston cylinder experiments. *Contrib. Mineral. Petrol.* **169**, 1–16 (2015).
38. Pichavant, M., Villaros, A., Michaud, J. A.-S. & Scaillet, B. Granite magmatism and mantle filiation. *Eur. J. Mineral.* **36**, 225–246 (2024).
39. Christiansen, E. H., Sheridan, M. F. & Burt, D. M. The geology and geochemistry of Cenozoic topaz rhyolites from the Western United States in Special paper 205, 1–82 (The Geological Society of America, 1986).
40. Linnen, R., McNeil, A. & Flemming, R. Some thoughts on metasomatism in pegmatites. *Can. Mineral.* **57**, 765–766 (2019).
41. Bucholz, C. E., Stolper, E. M., Eiler, J. M. & Breaks, F. W. A comparison of oxygen fugacities of strongly peraluminous granites across the Archean–Proterozoic boundary. *J. Petrol.* **59**, 2123–2156 (2018).
42. Shaw, D. M. Trace element fractionation during anatexis. *Geochim. Cosmochim. Acta.* **34**, 237–243 (1970).

43. Raimbault, L., Cuney, M., Azencott, C., Duthou, J. L. & Joron, J. L. Geochemical evidence for a multistage magmatic genesis of Ta–Sn–Li mineralization in the granite at Beauvoir, French Massif Central. *Econ. Geol.* **90**, 548–576 (1995).
44. Acosta-Vigil, A. et al. Mechanisms of crustal anatexis: a geochemical study of partially melted metapelitic enclaves and host dacite, SE Spain. *J. Petrol.* **51**, 785–821 (2010).
45. Padilla, A. J. & Gualda, G. A. R. Crystal-melt elemental partitioning in silicic magmatic systems: an example from the Peach Spring Tuff high-silica rhyolite, Southwest USA. *Chem. Geol.* **440**, 326–344 (2016).
46. Neukampf, J., Ellis, B. S., Magna, T., Laurent, O. & Bachmann, O. Partitioning and isotopic fractionation of lithium in mineral phases of hot, dry rhyolites: the case of the Mesa Falls Tuff, Yellowstone. *Chem. Geol.* **506**, 175–186 (2019).
47. Neukampf, J., Ellis, B. S., Magna, T., Laurent, O. & Marrocchi, Y. Partitioning and isotopic fractionation of Li between mineral phases and alkaline to calc-alkaline melts of explosive and effusive eruptions. *Chem. Geol.* **636**, 1–19 (2023).
48. Pichavant, M., Erdmann, S., Kontak, D. J., Michaud, J. A.-S. & Villaros, A. Trace element partitioning in strongly peraluminous rare-metal silicic magmas— implications for fractionation processes and for the origin of the Macusani Volcanics (SE Peru). *Geochim. Cosmochim. Acta* **365**, 229–252 (2024).
49. Jolliff, B. L., Papike, J. J. & Shearer, C. K. Petrogenetic relationships between pegmatite and granite based on geochemistry of muscovite in pegmatite wall zones, Black Hills, South Dakota, USA. *Geochim. Cosmochim. Acta* **56**, 1915–1939 (1992).
50. Simons, B., Andersen, J. C. Ø, Shail, R. K. & Jenner, F. E. Fractionation of Li, Be, Ga, Nb, Ta, In, Sn, Sb, W and Bi in the peraluminous Early Permian Variscan granites of the Cornubian Batholith: precursor processes to magmatic-hydrothermal mineralisation. *Lithos* **278–281**, 491–512 (2017).
51. Dohmen, R. & Blundy, J. A predictive thermodynamic model for element partitioning between plagioclase and melt as a function of pressure, temperature and composition. *Am. J. Sci.* **314**, 1319–1372 (2014).
52. Prowatke, S. & Klemme, S. Rare earth element partitioning between titanite and silicate melts: Henry's law revisited. *Geochim. Cosmochim. Acta.* **70**, 4997–5012 (2006).
53. Ellis, B. S. et al. Biotite as a recorder of an exsolved Li-rich volatile phase in upper-crustal silicic magma reservoirs. *Geology* **50**, 481–485 (2022).
54. Torró, L. et al. Lithium mica clasts document magmatic evolution prior to eruption in the Macusani volcanic field in Peru. *Sci. Rep.* **15**, 1–16 (2025).
55. Černý, P. et al. Lithium in sekaninaite from the type locality, Dolní Bory, Czech Republic. *Can. Mineral.* **35**, 167–173 (1997).
56. Tailby, N. D., Cherniak, D. J. & Watson, B. E. Al diffusion in quartz. *Am. Mineral.* **103**, 839–847 (2018).
57. Ramirez-Briones, J. S. et al. Petrogenesis of volcanogenic sedimentary lithium ore in the Neogene Macusani volcanic field, Puno, Peru. *J. Petrol.* **66**, 1–26 (2025).
58. Spear, F. S., Kohn, M. J. & Cheney, J. T. *P–T* paths from anatectic pelites. *Contrib. Mineral. Petrol.* **134**, 17–32 (1999).
59. García-Casco, A. et al. Synthesis of staurolite in melting experiments of a natural metapelite: consequences for the phase relations in low-temperature pelitic migmatites. *J. Petrol.* **44**, 1727–1757 (2003).
60. Konzett, J., Hauzenberger, C., Ludwig, T. & Stalder, R. Anatectic granitic pegmatites from the eastern Alps: a case of variable rare metal enrichment during high-grade regional metamorphism. II: Pegmatite staurolite as an indicator of anatectic pegmatite parent melt formation—a field and experimental study. *Can. Mineral.* **56**, 603–624 (2018).
61. Franceschelli, M., Puxeddu, M. & Memmi, I. Li, B-rich Rhaetian metabauxite, Tuscany, Italy: reworking of older bauxites and igneous rocks. *Chem. Geol.* **144**, 221–242 (1998).
62. Verlaguet, A. et al. Metamorphic veining and mass transfer in a chemically closed system: a case study in Alpine metabauxites (western Vanoise). *J. Metamorph. Geol.* **29**, 275–300 (2011).
63. Thomsen, T. B. & Schmidt, M. W. Melting of carbonated pelites at 2.5–5.0 GPa, silicate–carbonatite immiscibility, and potassium–carbon metasomatism of the mantle. *Earth Planet. Sci. Lett.* **267**, 17–31 (2008).
64. Bucholz, C. E. & Spencer, C. J. Strongly peraluminous granites across the Archean Proterozoic transition. *J. Petrol.* **60**, 1299–1348 (2019).
65. Černý, P. Fertile granites of Precambrian rare-element pegmatite fields: is geochemistry controlled by tectonic setting or source lithologies?. *Precambr. Res.* **51**, 429–468 (1991).
66. Smithies, R. H. et al. Giant lithium-rich pegmatites in Archean cratons form by remelting refertilised roots of greenstone belts. *Commun. Earth Environ.* **6**, 1–11 (2025).
67. Gion, A. M., Gaillard, F., Freslon, N., Erdmann, S. & Di Carlo, I. A method for the direct analysis of quenched, magmatic-hydrothermal fluids recovered from high-pressure, high-temperature experiments. *Chem. Geol.* **609**, 1–13 (2022).
68. Chen, J. et al. Melting conditions in the modern Tibetan crust since the Miocene. *Nat. Commun.* **9**, 1–13 (2018).
69. Van Achterbergh, E., Ryan, C. & Griffin, W. *GLITTER User's Manual: On-line Interactive Data Reduction for the LAICP-MS Microprobe, Version 4* https://www3.nd.edu/~asimonet/CE60342/Glitter_V4.4_manual.pdf (2001).
70. Lefebvre, G. & Tavignot, D. Le marché du lithium en 2020: enjeux et paradoxes. *MineralInfo* https://www.mineralinfo.fr/fr/ecomine/marche-du-lithium-2020-enjeux-paradoxes (2020).

Acknowledgements

Bence Horányi is supported by the ANR TRANSFAIR grant (ANR-21-CE01-0022), which was awarded to Jérémie Melleton. The authors were further supported by LabEx VOLTAIRE (ANR-10-LABX-100-01), EquipEx PLANEX (ANR-11-EQPX-0036), ANR MAGBRINES (ANR-24-CE49-6543), and the BRGM Incremental WSn projects (RP20DGR035 and RP21DGR035). This work has benefited from the facilities of the MACLE-CVL Platform, which was co-funded by the European Union and the Centre-Val de Loire Region (FEDER). David Sifré and Patricia Benoist are thanked for their assistance with piston-cylinder experiments and SEM analyses, respectively. Bruno Goffé and Christian Chopin are thanked for providing the Barr888 meta-bauxite. The authors are grateful for the constructive feedback of David London, Manuel Duguet, and Lisard Torró, as well as Lot Koopmans, Robert Linnen, and an anonymous reviewer on a previous iteration of the manuscript. Evan Hastie is thanked for the efficient editorial handling of the manuscript. Bence Horányi would also like to thank Michel Pichavant and Marieke van Lichtervelde for their insightful comments and discussions on the experimental results.

Author contributions

B.H.—experiments, analyses of run products, data curation, and manuscript preparation. A.M.G.—supervision and manuscript preparation. F.G.—project conceptualisation, resource management, supervision, and manuscript preparation. É.G.—project conceptualisation and supervision. A.P.—analyses of starting materials and supervision. J.M.—project conceptualisation, funding acquisition, resource management, and supervision. A.M.-C.—experiments and analyses of run products. J.G.—experiments, analyses of starting materials, and analyses of run products. S.E.—analyses of starting materials and analyses of run products. I.D.C.—analyses of starting materials and analyses of run products. The manuscript was reviewed and approved by all authors.

Competing interests
The authors declare no competing interests.

Additional information
Supplementary information The online version contains supplementary material available at https://doi.org/10.1038/s43247-025-02923-9.

Correspondence and requests for materials should be addressed to Bence Horányi.

Peer review information *Communications Earth & Environment* thanks David London, Manuel Duguet and Lisard Torro reviewer(s) for their contribution to the peer review of this work. Primary Handling Editors: Evan Hastie and Alireza Bahadori. A peer review file is available.